



Recycling carbon dioxide in the cement industry to produce added-value additives: a step towards a CO<sub>2</sub> circular economy

# Deliverable D6.3

## Report on individual units models

WP6 – Integrated Technology Modelling and Optimization

Version 3.0

**Authors:** Akrivi Asimakopoulou (CERTH), Dimitrios Koutsonikolas (CERTH), Michalis Mouratidis (CERTH), Grigorios Pantoleonos (CERTH), Theodoros Damartzis (CERTH), Georgios Skevis (CERTH)

**Lead participant:** CERTH

**Delivery date:** 31 October 2019


**Dissemination level:** Public

**Type:** Report




*This project has received funding from the European Union's Horizon 2020 Research and Innovation Programme under Grant Agreement No. 768583. The content of this publication is the sole responsibility of the authors. The European Commission or its services cannot be held responsible for any use that may be made of the information it contains.*



	Title <b>Report on the individual units models</b>	Deliverable number <b>D6.3</b>
		Version <b>3.1</b>


## Revision History


Author Name, Partner short name	Description	Date
Akrivi Asimakopoulou (CERTH) Dimitrios Koutsonikolas (CERTH), Michalis Mouratidis (CERTH), Grigorios Pantoleonos (CERTH), Georgios Skevis (CERTH)	Draft deliverable (version 1.0)	14/10/2019
Akrivi Asimakopoulou (CERTH) Dimitrios Koutsonikolas (CERTH), Michalis Mouratidis (CERTH), Grigorios Pantoleonos (CERTH), Georgios Skevis (CERTH)	Final version (2.0)	18/12/2019
Christian Mueller (DVGW)	Revised version (2.1)	17/1/2019
Akrivi Asimakopoulou (CERTH) Dimitrios Koutsonikolas (CERTH), Michalis Mouratidis (CERTH), Grigorios Pantoleonos (CERTH), Georgios Skevis (CERTH)	Final version and approval (3.0)	10/2/2020
Akrivi Asimakopoulou (CERTH) Dimitrios Koutsonikolas (CERTH), Michalis Mouratidis (CERTH), Grigorios Pantoleonos (CERTH), Theodoros Damartzis (CERTH), Georgios Skevis (CERTH)	Revised version (3.1)	30/6/2021

	Title Report on the individual units models	Deliverable number <b>D6.3</b>
		Version <b>3.1</b>

## Table of Contents

<b>Revision History.....</b>	<b>2</b>
<b>Table of Contents.....</b>	<b>3</b>
<b>1 Introduction .....</b>	<b>5</b>
<b>2 CO<sub>2</sub> absorption-desorption unit.....</b>	<b>6</b>
2.1 Solvents.....	6
2.2 Process simulation of the CO <sub>2</sub> purification unit.....	10
2.2.1 Absorption unit simulation .....	12
2.3 CFD modelling and simulation of the absorption unit.....	14
2.3.1 Model formulation.....	14
2.3.2 Model validation .....	18
2.3.3 Design and operational specifications of the absorption column model.....	20
2.3.4 Simulation results .....	23
2.3.4.1 Conclusions .....	26
<b>References.....</b>	<b>27</b>
<b>3 CaCO<sub>3</sub> precipitation unit .....</b>	<b>29</b>
3.1 Introduction .....	29
3.2 Aqueous electrolyte thermodynamics.....	30
3.3 Membrane crystallization technology .....	32
3.4 Results & Discussion .....	34
3.5 Conclusions & Outlook.....	38
<b>Appendix A - Coupling of Aspen Plus and gPROMS: the CAPE-OPEN standard .....</b>	<b>39</b>
Flash calculation example .....	39
<b>Appendix B - Additional equations for the membrane-based crystallization and method of solution ..</b>	<b>42</b>
<b>Nomenclature.....</b>	<b>44</b>
<b>References.....</b>	<b>46</b>
<b>4 Electrochemical cell model.....</b>	<b>49</b>
4.1 Results and discussion .....	52
4.2 Membrane characterization .....	53
4.3 Electrocatalyst characterization.....	54
<b>References.....</b>	<b>56</b>

	Title Report on the individual units models	Deliverable number <b>D6.3</b>
		Version <b>3.1</b>


	Title <b>Report on the individual units models</b>	Deliverable number <b>D6.3</b>
		Version <b>3.1</b>

## 1 Introduction

The present deliverable reports on the activities of Task 6.2 which involve the development of models and simulation methodologies for the key sub-units of the RECODE project namely (a) the CO<sub>2</sub> absorption-desorption unit, (b) the CaCO<sub>3</sub> precipitation unit and (c) the electrocatalytic units. The objective of the work is to develop and assess generic numerical methodologies, based on actual lab-scale units designed and operated by the project partners that can both accurately describe the key physical and chemical processes taking place as well to perform parametric studies leading to optimized sub-unit operation. The developed models will be continuously validated as updated data from the operation of the individual units become available and will form the basis for the development of a working system model for the complete pilot plant unit, to be presented in D6.4. The modelling and simulation methodologies for each unit are described in the Sections below.

The deliverable has been originally submitted on 10/2/2020. This current version (3.1, re-submitted) incorporates the following features

- (1) Updated ionic liquid (IL) physical and chemical properties as have become available within the project and re-evaluation of the detailed flow and reactive field in the DVGW mini-plant on the basis of the latter
- (2) Re-evaluation and validation of the electrochemical cell model.

	Title Report on the individual units models	Deliverable number <b>D6.3</b>
		Version <b>3.1</b>

## 2 CO<sub>2</sub> absorption-desorption unit

The objective of the work is to develop a working model for the simulation of the carbon dioxide capture process in an absorption column. The model follows the geometry, dimensions and setup of the DVGW mini plant, as described in detail in D3.3. However, the methodology is generic and can be applied to alternative designs and also be used for unit scale-up. A process schematic is shown in Figure 2.1.

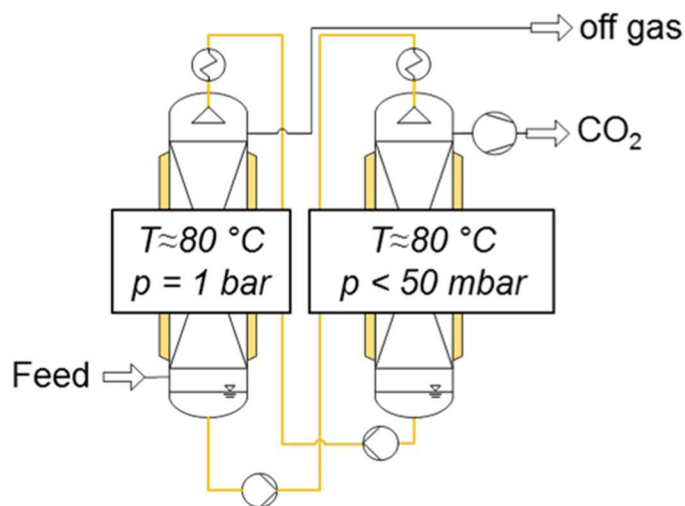



Figure 2.1: Process schematic of the DVGW mini plant

Three distinct modelling approaches are followed in this work

- (1) A thermodynamic and rate-based (0-D/1-D) simulation of the absorption-desorption unit suitable for plant techno-economic assessment and parametrization
- (2) An equilibrium process (0-D/1-D) model of the generic absorption-desorption unit suitable for scaling-up and optimization
- (3) A detailed (2-D/3-D) CFD model of the complex multiphase flow in the mini plant absorption unit.

### 2.1 Solvents

The choice of the appropriate absorbents for carbon capture is a key parameter in the operation of absorption-desorption units and its choice is determined by a range of diverse technical (e.g. flue gas composition, materials and environmental compatibility) and operational (e.g. cost, logistics) parameters. Amines, such as monoethanolamine (MEA), are considered the most promising near-term technological option [e.g. 1, 2]. The major drawback in the utilization of MEA, apart from its corrosive behavior and fairly rapid degradation, is the extensive energy consumption in the regeneration loop due to the high heat demands of the thermally driven desorber. In that sense the process integration performed in the context of the RECODE project is important as it will propose integration strategies to reduce energy requirements to an acceptable level. Ionic liquids, developed and utilized in the RECODE project, are organic salts with melting points close to or below room temperature and are characterized by high CO<sub>2</sub> solubility and low energy requirements for regeneration, enabled by the different mode of operation of the desorber (i.e. vacuum regeneration), together with high thermal stability and low volatility [e.g. 2, 3].

	Title <b>Report on the individual units models</b>	Deliverable number <b>D6.3</b>
		Version <b>3.1</b>

There is limited information regarding the physical and chemical properties of ILs with significant data generated within the RECODE project. Three solvents have been considered in the present work. Initially an aqueous MEA (monoethanolamine) solution obtained from the literature was used as a benchmark. Following that two ionic liquids used by DVGW for CO<sub>2</sub> purification in their mini plant were simulated i.e. a mixture (10:90 by weight) of [BDiMIM][Pro] (1-Butyl-2,3-dimethylimidazolium bis(trifluorsulfonyl)imide) in [BDiMIM][BTA] (1-butyl-3-methylimidazolium bis(trifluoromethylsulfonyl)imide) (referred to as BDiMIM for simplicity) and 1-Ethyl-3-methylimidazolium acetate referred to as [EMIM][OAc]. Selected properties for MEA are summarized in Table 2.1 while a review of IL properties is presented in Table 2.2.

*Table 2.1: Typical MEA and water physical properties [4]*

	MEA	Water
MW (kg/mol)	0.0611	0.018
Boiling point @ 760 mmHg (°C)	170.4	100
$\Delta H_{\text{vap}}$ (kJ/kg)	915.15	2453.5
$C_p$ (kJ/kgK)	2.757	4.182
Specific gravity @ 20 °C	1.017	1
Dynamic viscosity @ 20 °C (cP)	18.95	0.89
Surface tension (dynes/cm)	48.3	71.97



	Title Report on the individual units models	Deliverable number <b>D6.3</b>
		Version <b>3.1</b>

Table 2.2: Review of 10 wt-% [BDiMIM][Pro] in [BDiMIM][BTA] and [EMIM][OAc] properties

		10 wt-% [BDiMIM][Pro] in [BDiMIM][BTA]		[EMIM][OAc]	
		Value	Comments	Value	Comments
MW (kg/mol)	[BDiMIM][Pro]	0.267	DVGW Private Communication	0.1702	proionic.com
	[BDiMIM][BTA]	0.433	DVGW Private Communication		
Density (kg/m <sup>3</sup> )	[BDiMIM][Pro]	1300	DVGW Private Communication	$\rho$ = 1000 * (1.278 – 0.0006054 T)	Quijada-Maldonado et al., 2012 [6]
	[BDiMIM][BTA]	1400	DVGW Private Communication	$\rho$ = 1012.482 – 0.918103T + 6.25 * 10 <sup>–5</sup> T <sup>2</sup> + 758.0905ξ – 497.846ξ <sup>2</sup> + 0.302582Tξ	Aqueous solution with T [=] K ξ the EMIM mass fraction Qu et al., 2017 [7]
Heat capacity (J/kg/K)		2000 @25 °C	D3.3	2400	Ma et al., 2012 [8]
Heat capacity (kJ/kg/K)				$C_p$ = 2.761077 + 0.008120T – 1.106151 * 10 <sup>–5</sup> T <sup>2</sup> – 2.649514ξ – 0.918307ξ <sup>2</sup> + 0.003580Tξ	Aqueous solution with T [=] K ξ the EMIM mass fraction Qu et al., 2017 [7]
Vapor pressure (Pa)		negligible	Ortloff et al., 2018 [5]	negligible	Ortloff et al., 2018 [5]
				(see figure below)	Qu et al., 2017 [7]
Viscosity (mPas)		15 @80 °C	Ortloff et al., 2018 [5]	$e^{-1.621 + \frac{664.5}{T-196.1}}$	Quijada-Maldonado et al., 2012 [6]
				$\ln\eta$ = 3.025114 – 0.150834T + 2.20875 * 10 <sup>–4</sup> T <sup>2</sup> – 0.40864ξ – 9.363176ξ <sup>2</sup> + 0.03072Tξ	Aqueous solution with T [=] K ξ the EMIM mass fraction Qu et al., 2017 [7]
Reaction with CO <sub>2</sub>	E <sub>A</sub> (J/mol)	43830	Ortloff et al., 2018 [5]	10317	Zareiekordshouli et al., 2018 [9]
	ln(k <sub>0</sub> )	28.37 @ 25-60 °C	Ortloff et al., 2018 [5]	7.343	Zareiekordshouli et al., 2018 [9]
		25.944 @80 °C			



	Title Report on the individual units models	Deliverable number <b>D6.3</b>
		Version <b>3.1</b>

The variation of vapor pressure with temperature for the aqueous [EMIM][OAc] ionic liquid mixture is presented in Figure 2.2. It can be concluded that the vapor pressure of the pure [EMIM][OAc] solvent used for carbon dioxide absorption in our case is negligible.

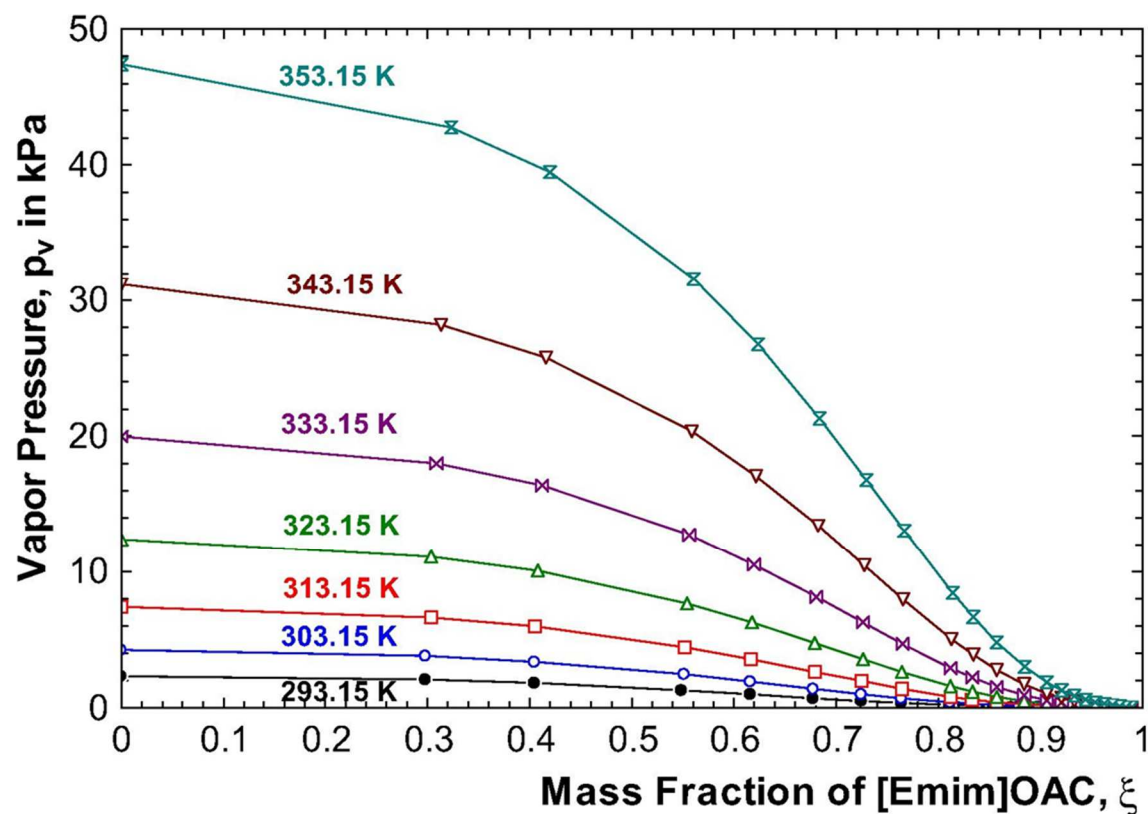


Figure 2.2: Vapor pressure of aqueous solution of [Emim]OAc as a function of it's mass fraction  $\xi$  and temperature (pure [Emim]OAc at  $\xi=1$ ) (from Qu et al., 2017)

## 2.2 Process simulation of the CO<sub>2</sub> purification unit

A working model of a state-of-the-art CO<sub>2</sub> absorption-desorption process has been assembled using the Aspen Plus® commercial process simulation software [10] and is outlined in Figure 2.3. The process is different from the RECODE process, since the amines are thermally regenerated instead of vacuum regenerated ILs, it can be used as benchmark for the techno-economic assessment of the RECODE process.

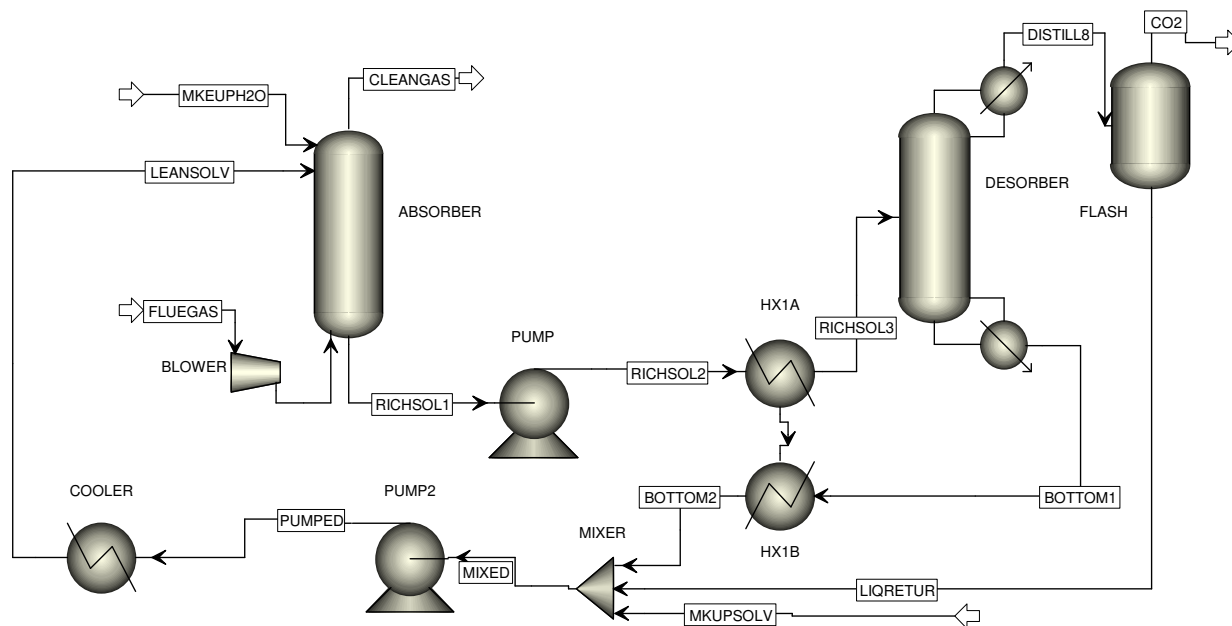


Figure 2.3: Layout of the CO<sub>2</sub> absorption-desorption process.

The working blocks used for the process simulation are: i) two packed columns for absorption and desorption (RadFrac columns, equilibrium mode of operation), ii) a flash drum for vapor-liquid separation (FLASH), iii) two pumps for liquid transport (PUMP), a blower to feed the flue gas in the column (BLOWER), iv) a mixing vessel to homogenize three different liquid streams (MIXER) and v) a series of heat exchangers to control process streams temperature (HX1A, HX1B). The simulations were performed using a typical TITAN flue gas composition as shown in Table 2.3.

Table 2.3: Typical flue gas composition

	Feed gas	CO <sub>2</sub>	H <sub>2</sub> O	O <sub>2</sub>	N <sub>2</sub>
%	100	16	8	14	62
kmol/h (basis)	800	128	64	112	496

A working basis was arbitrarily selected for feed gas flow, but all generated data are valid for any other flow since they can be expressed relevant to this basis. The simulation provides the mass and energy balances of the whole process, as well as working data for each block used. Detailed information for every process stream depicted in Figure 2.3 can be found in Table 2.4.


	<b>Title</b> <b>Report on the individual units models</b>	<b>Deliverable number</b> <b>D6.3</b>
		<b>Version</b> <b>3.1</b>

Table 2.4: Detailed data for all process streams

	Units	BOTTOM1	BOTTOM2	CLEANGAS	CO2	DISTILL8	FEEDGAS	FLUEGAS	LEANSOLV	LIQRETUR	MIXED	MKEUPH2CMKUPSOLV	PUMPED	RICHXSOL1	RICHXSOL2	RICHXSOL3	
Description																	
From		STRIPPER	HX1B	ABSORBER	FLASH	STRIPPER	BLOWER		COOLER	FLASH	MIXER			PUMP2	ABSORBER	PUMP	HX1A
To		HX1B	MIXER			FLASH	ABSORBER	BLOWER	ABSORBER	MIXER	PUMP2	ABSORBER	MIXER	COOLER	PUMP	HX1A	STRIPPER
Phase		Liquid	Liquid	Vapor	Vapor	Vapor	Vapor	Vapor	Liquid	Liquid	Liquid	Liquid	Liquid	Liquid	Liquid	Liquid	Mixed
Temperature	C	106,4351	92,03642	53,366093	35	96,17281	76,2425	70	37	35	79,27731	37	38	79,09434	68,47189	68,47349	80
Pressure	bar	1,05	1,05	1	1	1	1,05	1	1,08	1	1	1,08	1	1,08	1,05	1,1	1,05
Molar Vapor Fraction		0	0	1	1	1	1	1	0	0	0	0	0	0	0	0	3,06E-06
Molar Liquid Fraction		1	1	0	0	0	0	0	1	1	1	1	1	1	1	1	0,999997
Molar Solid Fraction		0	0	0	0	0	0	0	0	0	0	0	0	0	0	0	0
Mass Vapor Fraction		0	0	1	1	1	1	1	0	0	0	0	0	0	0	0	3,59E-06
Mass Liquid Fraction		1	1	0	0	0	0	0	1	1	1	1	1	1	1	1	0,999996
Mass Solid Fraction		0	0	0	0	0	0	0	0	0	0	0	0	0	0	0	0
Molar Enthalpy	kcal/mol	-67,1598	-67,45857	-8,280504	-91,8936	-61,5737	-19,2945	-19,341	-68,46166	-68,1462	-67,6382	-68,0956	-64,39855	-67,6381	-69,3919	-69,3919	-69,1775
Mass Enthalpy	kcal/kg	-2685,49	-2697,434	-304,6715	-2160,92	-2913,55	-636,13	-637,665	-2948,017	-3779,9	-2912,56	-3779,88	-1054,267	-2912,55	-2901,73	-2901,73	-2892,77
Molar Entropy	cal/mol-K	-56,3507	-56,86524	0,7566958	0,79684	-6,75033	2,483484	2,445838	-54,52236	-38,3705	-52,0353	-38,2615	-118,194	-52,0462	-69,9189	-69,9188	-69,1505
Mass Entropy	cal/gm-K	-2,25327	-2,273843	0,0278417	0,018738	-0,31941	0,081879	0,080638	-2,347779	-2,12831	-2,24068	-2,12383	-1,934951	-2,24116	-2,92377	-2,92377	-2,89164
Molar Density	mol/cc	0,036972	0,037495	3,69E-05	3,92E-05	3,28E-05	3,62E-05	3,51E-05	0,0423168	0,055094	0,04107	0,055143	0,0165165	0,041076	0,039055	0,039055	0,038644
Mass Density	kg/cum	924,622	937,6958	1,0022036	1,667814	0,692808	1,097307	1,064089	982,72157	993,2746	953,7557	993,4246	1008,8873	953,9009	933,9549	933,9553	924,1277
Enthalpy Flow	Gcal/hr	-182,569	-183,3817	-5,899406	-12,4641	-65,8895	-15,4356	-15,4728	-250,0819	-63,6796	-247,074	-3,27518	-9,38E-05	-247,074	-262,893	-262,893	-262,081
Average MW		25,00842	25,00842	27,178465	42,52525	21,13358	30,33098	30,33098	23,222954	18,02859	23,22295	18,01528	61,08372	23,22295	23,1395	23,1395	23,1395
Mole Flows	kmol/hr	2718,434	2718,434	712,4453	135,6361	1070,093	800	800	3652,8753	934,4565	3652,875	48,09686	0,0014562	3652,875	3788,527	3788,527	3788,527
CO2	kmol/hr	53,26451	53,26451	0,1178279	127,8853	128,3281	128	128	53,710438	0,442754	53,71044	0	0	53,71044	181,5926	181,5926	181,5926
H2O	kmol/hr	2255,918	2255,918	104,33669	7,740089	941,7323	64	64	3189,8906	933,9922	3189,891	48,09686	0	3189,891	3197,651	3197,651	3197,651
O2	kmol/hr	5,74E-50	5,74E-50	111,99696	0,003038	0,003039	112	112	4,11E-07	4,11E-07	4,11E-07	0	0	4,11E-07	0,003039	0,003039	0,003039
N2	kmol/hr	8,56E-52	8,56E-52	495,99236	0,007636	0,007637	496	496	5,39E-07	5,39E-07	5,39E-07	0	0	5,39E-07	0,007637	0,007637	0,007637
MEA	kmol/hr	409,2514	409,2514	0,0014562	4,78E-11	0,021542	0	0	409,27435	0,021542	409,2744	0	0,0014562	409,2744	409,2729	409,2729	409,2729
Mole Fractions																	
CO2		0,019594	0,019594	0,0001654	0,942856	0,119922	0,16	0,16	0,0147036	0,000474	0,014704	0	0	0,014704	0,047932	0,047932	0,047932
H2O		0,829859	0,829859	0,1464487	0,057065	0,880047	0,08	0,08	0,8732547	0,999503	0,873255	1	0	0,873255	0,844035	0,844035	0,844035
O2		2,11E-53	2,11E-53	0,1572008	2,24E-05	2,84E-06	0,14	0,14	1,12E-10	4,40E-10	1,12E-10	0	0	1,12E-10	8,02E-07	8,02E-07	8,02E-07
N2		3,15E-55	3,15E-55	0,6961831	5,63E-05	7,14E-06	0,62	0,62	1,48E-10	5,77E-10	1,48E-10	0	0	1,48E-10	2,02E-06	2,02E-06	2,02E-06
MEA		0,150547	0,150547	2,04E-06	3,53E-13	2,01E-05	0	0	0,1120417	2,31E-05	0,112042	0	1	0,112042	0,10803	0,10803	0,10803
Mass Flows	kg/hr	67983,76	67983,76	19363,17	5767,959	22614,89	24264,78	24264,78	84830,557	16846,93	84830,56	866,4784	0,0889517	84830,56	90598,65	90598,65	90598,65
CO2	kg/hr	2344,16	2344,16	5,1855806	5628,208	5647,694	5633,254	5633,254	2363,7856	19,48553	2363,786	0	0	2363,786	7991,854	7991,854	7991,854
H2O	kg/hr	40641	40641	1879,6547	139,4399	16965,57	1152,978	1152,978	57466,771	16826,13	57466,77	866,4784	0	57466,77	57606,57	57606,57	57606,57
O2	kg/hr	1,84E-48	1,84E-48	3583,7684	0,097217	0,09723	3583,866	3583,866	1,31E-05	1,31E-05	1,31E-05	0	0	1,31E-05	0,09723	0,09723	0,09723
N2	kg/hr	2,40E-50	2,40E-50	13894,472	0,213915	0,21393	13894,69	13894,69	1,51E-05	1,51E-05	1,51E-05	0	0	1,51E-05	0,21393	0,21393	0,21393
MEA	kg/hr	24998,6	24998,6	0,0889517	2,92E-09	1,315847	0	0	25000	1,315847	25000	0	0,0889517	25000	24999,91	24999,91	24999,91
Mass Fractions																	
CO2		0,034481	0,034481	0,0002678	0,975771	0,249733	0,232158	0,232158	0,0278648	0,001157	0,027865	0	0	0,027865	0,088212	0,088212	0,088212
H2O		0,597805	0,597805	0,0970737	0,024175	0,750195	0,047517	0,047517	0,6774301	0,998765	0,67743	1	0	0,67743	0,635844	0,635844	0,635844
O2		2,70E-53	2,70E-53	0,1850817	1,69E-05	4,30E-06	0,147698	0,147698	1,55E-10	7,80E-10	1,55E-10	0	0	1,55E-10	1,07E-06	1,07E-06	1,07E-06
N2		3,53E-55	3,53E-55	0,7175722	3,71E-05	9,46E-06	0,572628	0,572628	1,78E-10	8,97E-10	1,78E-10	0	0	1,78E-10	2,36E-06	2,36E-06	2,36E-06
MEA		0,367714	0,367714	4,59E-06	5,06E-13	5,82E-05	0	0	0,2947051	7,81E-05	0,294705	0	1	0,294705	0,275941	0,275941	0,275941
Volume Flow	cum/hr	73,526	72,50086	19320,596	3458,395	32642,37	22113,04	22803,35	86,322066	16,961	88,9437	0,872214	8,82E-05	88,93016	97,00538	97,00534	98,03694

Table 2.5 shows the heat duty in the process' blocks. This confirms that the most energy intensive part of the process is the amine regeneration process.

Table 2.5: Calculated heat duty of process blocks

Heat duty (kW)					
STRIPPER-REB	STRIPPER-COND	HEX1	FLASH	HEX2	COOLER
22.02	-6.18	0.94	-11.86	-0.94	-3.49

A snapshot of the process focusing only on the absorption-desorption unit is shown in Figure 2.4. Table 2.6 shows the overall process efficiency in terms of CO<sub>2</sub> recovery and CO<sub>2</sub> purity. The designed process scheme offers almost complete CO<sub>2</sub> recovery with very high CO<sub>2</sub> purity (~95%) which can be easily enhanced to >99% by cooling the stream and condensing the water vapor.

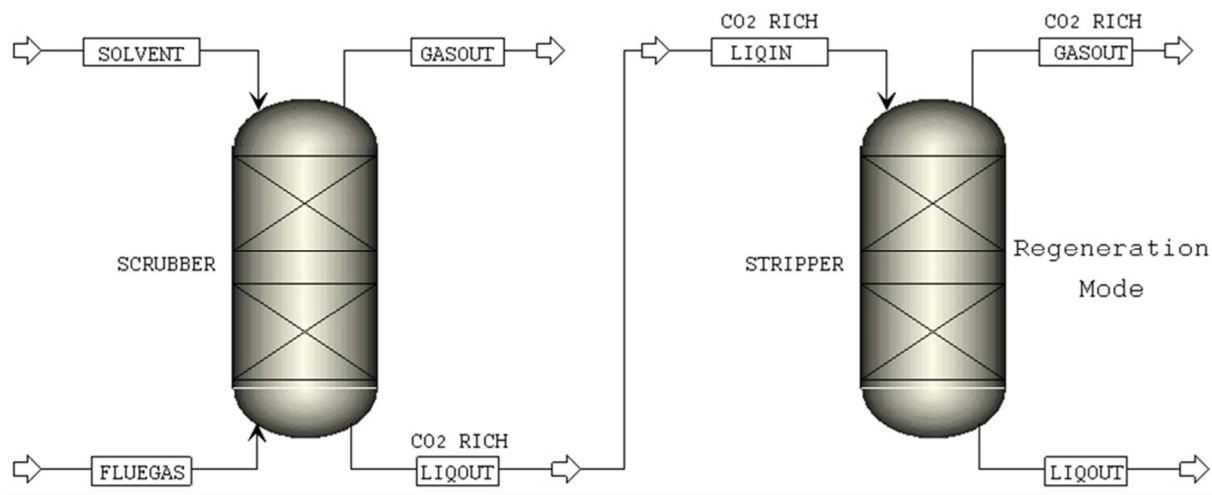


Figure 2.4: Layout of the absorption-desorption unit (detail)


Table 2.6: Summary of the process efficiency parameters

	Lean solvent	Rich solvent
Flow rate (kmol/h)	61.08	18.02
MEA concentration (M)	170.4	100
MEA load (mol CO <sub>2</sub> /mol MEA)	0.13	0.44
CO <sub>2</sub> recovery (kmol/h)		CO <sub>2</sub> recovery (%)
127.8		99.8
CO <sub>2</sub> purity: 95% (5% H <sub>2</sub> O @ 35 °C)		

### 2.2.1 Absorption unit simulation

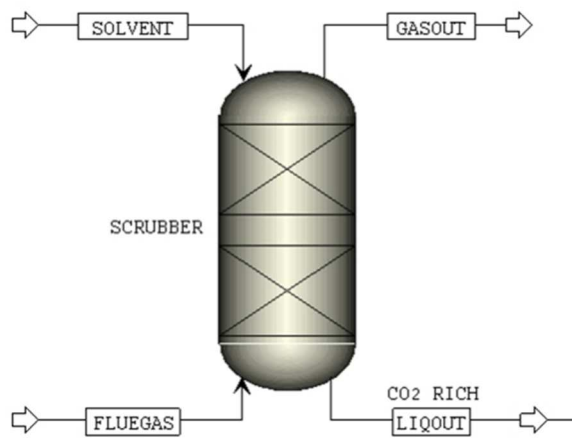
The CO<sub>2</sub> absorption unit developed at DVGW of a cylindrical column of 2 m height with two packing stages, 0.8 m each, filled with standard 8mm Raschig rings. The liquid phase (solvent) is introduced by a distributor plate through 25 holes of 2 mm diameter at the top of the cylinder while the CO<sub>2</sub>-rich flue gas stream is introduced counter-currently from the bottom. Both phases pass through the packed bed where the bulk of mass transfer and reaction takes place due to the enhanced contact surface. The liquid solvent is redistributed between the two packing stages. The column is operated at atmospheric pressure and at a temperature of 85 °C.

The absorber can be simulated in ASPEN using either a 0-D process model employing equilibrium or a 1D rate-based model. In this study the latter is used. This approach can provide very accurate conversion and process efficiency estimation provided that equilibrium thermodynamic and overall mass transfer correlations are known for each solvent. An outline of the absorber unit as modelled in Aspen Plus with operating parameters are summarized in Table 2-8. The absorber is modelled as a packed absorption column. The packing material provides the interphase for gas-liquid contact/reaction. The spray-packing interaction is represented by the number and location of stages. Mass transfer rates are calculated taking

	Title Report on the individual units models	Deliverable number <b>D6.3</b>
		Version <b>3.1</b>


explicitly into account the presence of chemical reactions. Case-specific design parameters (packing material, surface area, void fraction, etc) are used leading to a real-case representation. The single unit modeling with the rate based approach in Aspen Plus process simulator, except of absorption efficiency, can also provide data for column's hydraulics, e.g. flooding, foaming, etc.

Table 2.7: Absorber geometrical configuration and operating parameters

	<b>Dimensions (m x m)</b>	2 x 0.07
	<b>Number of packing stages</b>	2
	<b>Packing stage height (m)</b>	0.8
	<b>Type of packing material</b>	Raschig rings, 8mm
	<b>Hydraulic diameter (mm)</b>	70
	<b>Void fraction</b>	0.4
	<b>Pressure (bar)</b>	1
	<b>Temperature (°C)</b>	85
	<b>Flue gas inlet flow rate (lt/hr)</b>	100-200
	<b>IL pump around flow rate (lt/hr)</b>	10-40
	<b>Flue gas composition (N<sub>2</sub>, % vol.)</b>	50-85
	<b>Flue gas composition (CO<sub>2</sub>, % vol.)</b>	15-50

A typical simulation based on a flue gas (20% CO<sub>2</sub> by volume in N<sub>2</sub>) inlet flow rate of 250 lt/hr and a solvent (5% w/w aqueous MEA solution) flow rate of 10 lt/hr indicates a CO<sub>2</sub> recovery rate of 75%.

Extension of the above modelling approach to the RECODE process pre-supposes the availability of detailed rate data both for the mass transfer and chemical reaction processes involving ILs, which are currently unavailable. As a result two additional, complementary modelling approaches are implemented: an *equilibrium* process model which dispenses with the need for rate data (and detailed geometrical representation) and a detailed CFD approach where experimentally determined overall mass transfer and reaction rate data are coupled with mass, momentum, energy and species conservation equations integrated over a realistic geometry domain. The former approach is discussed in detail in D6.4 as it is primarily used for the integration of the CO<sub>2</sub> purification unit with the CO<sub>2</sub> utilization process in the RECODE demo plant. The latter is discussed in detail in the following section.

	Title <b>Report on the individual units models</b>	Deliverable number <b>D6.3</b>
		Version <b>3.1</b>

## 2.3 CFD modelling and simulation of the absorption unit

The absorption column was modelled using a 2-D/3-D Computational Fluid Dynamics (CFD) approach. CFD calculations can provide useful detailed information on the characteristics (velocity, turbulence intensity, pressure, etc) of the complex, multiphase flow field and quantify important design parameters such as the gas-liquid interfacial area, the volumetric mass transfer coefficients, the pressure drop across the packed bed, the gas or liquid holdup etc. Computations can also be used to predict wall wetting and propose alternative design configurations that will prolong reactor life and operation.

### 2.3.1 Model formulation

Two complementary modelling methodologies have been initially considered for the simulation of the complex flow field in the absorption column, using the ANSYS Fluent software [11]. The Eulerian-Eulerian approach (Mixture Model and Eulerian Multiphase Model in Fluent) assumes both gaseous and liquid phases as continuous fluids while the Eulerian-Lagrangian approach (Discrete Phase Model in Fluent) assumes a continuous primary phase and a dispersed secondary phase (droplets). There are distinct advantages and drawbacks in both methods. The Eulerian-Lagrangian approach can predict fluid-droplet interaction and histories, in dilute flows, thus explicitly quantify and potentially optimize distributor plate geometry and nozzle design. However, the model cannot, for example, accurately describe the two-phase interaction inside the porous zone neither can treat dense flows and is not considered further here.

In the Mixture Model (MM) Eulerian-Eulerian approach the continuity, momentum and energy equations are solved for the mixture, volume fraction equations are solved for the primary and secondary phases and a relative (slip) velocity is specified through an algebraic expression. As a result in the flow domain the phases share mixture averaged density, velocity, pressure, etc. It is worth mentioning that although MM takes relative velocities of the phases into consideration, it is assumed that local equilibrium is reached over a short spatial length.

The momentum equation for the mixture composed of  $n$ -phases is cast as

$$\frac{\partial}{\partial t}(\rho_m \vec{v}_m) + \nabla \cdot (\rho_m \vec{v}_m \vec{v}_m) = -\nabla p + \nabla \cdot [\mu_m (\nabla \vec{v}_m + \nabla \vec{v}_m^T)] + \rho_m \vec{g} + \vec{F} + \nabla \cdot \left( \sum_{k=1}^n \alpha_k \rho_k \vec{v}_{dr,k} \vec{v}_{dr,k} \right) \quad (2.1)$$

where  $\alpha_k$  is the  $k$ -phase volume fraction,  $\vec{u}_m$  is the mass averaged velocity defined as

$$\vec{u}_m = \frac{\sum_{k=1}^n \alpha_k \rho_k \vec{v}_k}{\rho_m}, \quad (2.2)$$

$\vec{v}_{dr,k}$  is the drift velocity for secondary phase  $k$ , calculated by

$$\vec{v}_{dr,k} = \vec{v}_k - \vec{v}_m \quad (2.3)$$

and  $\rho_m$  is the mixture density given by averaging for all existing phases and therefore

$$\rho_m = \sum_{k=1}^n \alpha_k \rho_k. \quad (2.4)$$

The continuity equation for the mixture is expressed as

	Title <b>Report on the individual units models</b>	Deliverable number <b>D6.3</b>
		Version <b>3.1</b>

$$\frac{\partial}{\partial t}(\rho_m) + \nabla \cdot (\rho_m \vec{v}_m) = 0, \quad (2.5)$$

while the energy equation for the mixture is formed as

$$\frac{\partial}{\partial t} \sum_{k=1}^n (\alpha_k \rho_k E_k) + \nabla \cdot \sum_{k=1}^n (\alpha_k \vec{v}_k (\rho_k E_k + p)) = \nabla \cdot (k_{eff} \nabla T) + S_E \quad (2.6)$$

where  $k_{eff} = \sum_{k=1}^n (\alpha_k (k_k + k_t))$  is the effective conductivity,  $k_t$  is the turbulent conductivity and for every  $k$ -phase

$$E_k = h_k + \frac{p}{\rho_k} + \frac{v_k^2}{2}. \quad (2.7)$$

The volume fraction equation solved for every secondary phase  $k$  is given by

$$\frac{\partial}{\partial t} (\alpha_k \rho_k) + \nabla \cdot (\alpha_k \rho_k \vec{v}_m) = -\nabla \cdot (\alpha_k \rho_k \vec{v}_{dr,k}) + \sum_{p=1}^n (\dot{m}_{pk} - \dot{m}_{kp}) \quad (2.8)$$

On the other hand in the Eulerian Multiphase Model (EMM) each phase is treated separately. Therefore, the conservation equations of continuity, momentum and energy are solved for all  $n$ -phases individually maintaining their own flow characteristics. However, a basic assumption in this model is that the pressure is shared by all phases.

In the EMM assuming that  $\alpha_q$  is the volume fraction of the  $q$ -phase, the momentum equation is formed as

$$\frac{\partial}{\partial t} (\alpha_q \rho_q \vec{v}_q) + \nabla \cdot (\alpha_q \rho_q \vec{v}_q \vec{v}_q) = -\alpha_q \nabla p + \nabla \cdot \bar{\tau}_q + \alpha_q \rho_q \vec{g} + \sum_{p=1}^n (K_{pq} (\vec{v}_p - \vec{v}_q) + \dot{m}_{pq} \vec{v}_{pq} - \dot{m}_{qp} \vec{v}_{qp}) + (\vec{F}_q + \vec{F}_{lift,q} + \vec{F}_{vm,q}). \quad (2.9)$$

The energy is conserved by solving the enthalpy equation for every  $q$ -phase as

$$\frac{\partial}{\partial t} (\alpha_q \rho_q h_q) + \nabla \cdot (\alpha_q \rho_q \vec{v}_q h_q) = \alpha_q \frac{\partial p_q}{\partial t} + \bar{\tau}_q : \nabla \vec{v}_q - \nabla \vec{q}_q + S_q + \sum_{p=1}^n (Q_{pq} + \dot{m}_{pq} h_{pq} - \dot{m}_{qp} h_{qp}). \quad (2.10)$$

The continuity equation is used so as to obtain the volume fraction for each fluid phase described by

$$\frac{1}{\rho_{rq}} \left( \frac{\partial}{\partial t} (\alpha_q \rho_q) + \nabla \cdot (\alpha_q \rho_q \vec{v}_q) \right) = \sum_{p=1}^n (\dot{m}_{pq} - \dot{m}_{qp}), \quad (2.11)$$

where  $\rho_{rq}$  is the  $q$ -phase reference density or the volume-averaged density.

In each phase, together with continuity, momentum and energy equations, the species mass transfer equations are solved. The latter are defined for each species  $i$  in  $q$ -phase as

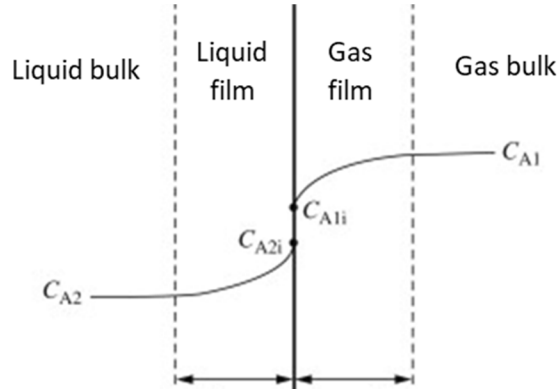
$$\frac{\partial (\alpha_q \rho_q Y_q^i)}{\partial t} + \nabla \cdot (\alpha_q \rho_q \vec{V}_q Y_q^i) = -\nabla \cdot (\alpha_q \vec{J}_q^i) + \alpha_q R_q^i + \alpha_q S_q^i + \sum_{p=1}^n \dot{m}_{p \rightarrow q}^i, \quad (2.12)$$

where  $Y_q^i$  is the mass fraction of species in the  $q$ -phase, the  $R_q^i$  is the net production rate due to chemical reaction and  $S_q^i$  is the production rate from external sources (which is not applicable in this simulation). Finally,  $\dot{m}_{p \rightarrow q}^i$  is the source term due to mass transfer from  $j$ -species in  $p$ -phase to  $i$ -species in  $q$ -phase.



	Title Report on the individual units models	Deliverable number <b>D6.3</b>
		Version <b>3.1</b>

The source term due to mass transfer is modeled with the two-film theory concept, which is graphically represented in the figure below.



From the two-film theory, the following expression is resulted, which relates the mass transfer source between the phases,  $\dot{m}_{p^i q^j}$ , the mass transfer coefficient for  $p$ -phase,  $k_p$ , and  $q$ -phase,  $k_q$ , the overall one,  $k_{pq}$ , the equilibrium ratio for molar concentration,  $K_{q^i p^j}$ , and the difference in concentration of the species in the phases

$$\dot{m}_{p^i q^j} = k_{pq} A_i (K_{q^i p^j} c_p^j - c_q^i) \quad (2.13)$$

$$\frac{1}{k_{pq}} = \frac{1}{k_q} + \frac{K_{q^i p^j}}{k_p}. \quad (2.14)$$

The mass transfer for each phase and the equilibrium ratio are parameters defined by the user, of which the latter is modeled with the Henry's Law combined with the Dalton's Law according to the following expression

$$K_{q^i p^j} = \frac{c_{p,e}}{c_{q,e}} \frac{P}{H^x} \quad (2.15)$$

where  $c_{p,e}$  and  $c_{q,e}$  are the equilibrium concentration of the species in  $p$  and  $q$ - phases and  $H^x$  is the Henry's coefficient for the species in the liquid phase.

The net production rate due to chemical reaction,  $R_q^i$ , is defined by

$$R_q^i = MW_i \sum_{r=1}^{N_r} (\hat{R}_{i,r}) \quad (2.16)$$

where  $N_r$  is the total number of reactions and  $\hat{R}_{i,r}$  is the molar rate of creation/destruction of species  $i$  in reaction  $r$  calculated by

$$\hat{R}_{i,r} = (v_{i,r}' - v_{i,r}'') \left( k_{f,r} \prod_{j=1}^N [C_{j,r}]^{\eta_{j,r}'} - k_{b,r} \prod_{j=1}^N [C_{j,r}]^{\eta_{j,r}''} \right) \quad (2.17)$$

where for reaction  $r$   $v_{i,r}'$  and  $v_{i,r}''$  are stoichiometric coefficient for reactant and product respectively,  $\eta_{j,r}'$  and  $\eta_{j,r}''$  are the rate exponents for reactant species  $j$  and  $C_{j,r}$  is the molar concentration of species  $j$ .



	Title <b>Report on the individual units models</b>	Deliverable number <b>D6.3</b>
		Version <b>3.1</b>

When the fluids are flowing through a porous zone – inside the packed beds – the conservation equations are slightly altered to incorporate the porous zone influence to the multiphase flow. For the multiphase flow inside porous media, considering that  $\varepsilon$  is the porous zone porosity, the continuity, momentum and energy equations are expressed as the Eq. (2.18), Eq. (2.19) and Eq. (2.20) respectively.

$$\frac{\partial}{\partial t}(\varepsilon a_q \rho_q) + \nabla \cdot (a \varepsilon_q \rho_q \vec{v}_q) = \sum_{p=1}^n (\dot{m}_{pq} - \dot{m}_{qp}) + \varepsilon S_q, \quad (2.18)$$

$$\begin{aligned} \frac{\partial}{\partial t}(\gamma \varepsilon_q \rho_q \vec{v}_q) + \nabla \cdot (\varepsilon a_q \rho_q \vec{v}_q \vec{v}_q) = & -\varepsilon a_q \nabla p + \nabla \cdot (\varepsilon \bar{\tau}_q) + \varepsilon a_q \rho_q \vec{B}_f - \left( \varepsilon^2 \alpha_q^2 \frac{\mu_q \vec{v}_q}{a K_{r,q}} + \right. \\ & \left. \varepsilon^3 \alpha_q^3 \frac{C_2 \rho_q |\vec{v}_q| \vec{v}_q}{2} \right) + \varepsilon \sum_{p=1}^n (K_{pq}(\vec{v}_p - \vec{v}_q) + \dot{m}_{pq} \vec{v}_{pq} - \dot{m}_{qp} \vec{v}_{qp}) + \varepsilon (\vec{F}_q + \vec{F}_{lift,q} + \vec{F}_{vm,q}). \end{aligned} \quad (2.19)$$

$$\begin{aligned} \frac{\partial}{\partial t} \left( a_q (\varepsilon \rho_q h_q - (1 - \varepsilon) \rho_s h_s) \right) + \nabla \cdot (\varepsilon a_q \rho_q \vec{v}_q h_q) = & -\varepsilon a_q \frac{\partial p_q}{\partial t} + \varepsilon \bar{\tau}_q : \nabla \vec{v}_q - \nabla \cdot \{ a_q [\varepsilon k_q + (1 - \varepsilon) k_s] \nabla T_q \} \\ & + \varepsilon S_q + \varepsilon \sum_{p=1}^n (Q_{pq} + \dot{m}_{pq} h_{pq} - \dot{m}_{qp} h_{qp}). \end{aligned} \quad (2.20)$$

A porous zone can introduce significant alterations in the hydrodynamic behavior such as static pressure rise due to diffusion and reduction in the flow energy, depending on the porous medium permeability, thereby making it more laminar. In the present work, where spatially-averaged flow characteristics are sufficient, a meso-scale approach is adopted and the packed regions of the absorption column are modelled through a Momentum Sink Approach (MSA, Porous Zone in Fluent) [11]. The momentum source term, assuming isotropic porous medium, is given by the expression

$$S_i = - \left( \frac{\mu}{\alpha} v_i + C_2 \frac{1}{2} \rho |v| v_i \right) \quad (2.21)$$

which is composed of a viscous loss term (first term) and an inertial loss term (second term). The viscous loss term corresponds to Darcy's Law, while the inertial loss term introduces inertial effects for large velocities. In the above equation  $\alpha$  is the permeability of the porous medium and  $C_2$  the inertial loss coefficient [e.g. 13].

The permeability and inertial loss coefficient can be estimated by semi-empirical correlations (e.g. Ergun's law) [e.g. 14], with  $D_p$  being the average diameter of the packing medium.

$$\frac{\Delta p}{L} = \frac{150 \mu (1 - \varepsilon)^2}{D_p^2 \varepsilon^3} v_\infty + \frac{1.75 \rho (1 - \varepsilon)}{D_p \varepsilon^3} v_\infty^2 \quad (2.22)$$

The randomly packed zone can also be simulated through Particle-Resolved Direct Numerical Simulation (PR-DNS) which relies on an accurate microscale representation of bed geometry and high grid resolution for reliable solution of flow between individual packed particles. Recent work [12] has shown that the PR-DNS approach is clearly superior to the MSA approach in predicting velocity fields when the flow enters the packed bed in a highly non-uniform manner. However, even in that case, the average pressure profile is satisfactorily predicted.

	Title <b>Report on the individual units models</b>	Deliverable number <b>D6.3</b>
		Version <b>3.1</b>

It should further be noted here that the assumption of isotropic porous medium can be readily relaxed by assuming varying resistances along different directions as well as networks of porous zones with variable spatial distribution.

The Reynolds Averaged Navier-Stokes (RANS) model was selected for modelling the internal turbulent flow of the absorption column. More specifically the standard two-equation k-ε turbulence model was used for all multiphase approaches. The standard k-ε turbulence model is a semi-empirical model where k stands for kinetic energy and ε for dissipation rate and are calculated by the following equations.

$$\frac{\partial}{\partial t}(\rho k) + \frac{\partial}{\partial x_i}(\rho k u_i) = \frac{\partial}{\partial x_j} \left[ \left( \mu + \frac{\mu_t}{\sigma_k} \right) \frac{\partial k}{\partial x_j} \right] + G_k + G_b - \rho \varepsilon - Y_M + S_k, \quad (2.20)$$

and

$$\frac{\partial}{\partial t}(\rho \varepsilon) + \frac{\partial}{\partial x_i}(\rho \varepsilon u_i) = \frac{\partial}{\partial x_j} \left[ \left( \mu + \frac{\mu_t}{\sigma_\varepsilon} \right) \frac{\partial \varepsilon}{\partial x_j} \right] + C_{1\varepsilon} \frac{\varepsilon}{k} (G_k + C_{3\varepsilon} G_b) - C_{2\varepsilon} \rho \frac{\varepsilon^2}{k} + S_\varepsilon, \quad (2.21)$$


where  $Y_M$  is the effect of compressible flow turbulence dilatation to the overall dissipation rate,  $C_{1\varepsilon}$ ,  $C_{2\varepsilon}$  and  $C_{3\varepsilon}$  are constants and  $S_k$ ,  $S_\varepsilon$  are user-defined turbulence source terms. Then, turbulent viscosity is calculated by the expression (2.18) where  $C_\mu$  is a given constant.

$$\mu_t = \rho C_\mu \frac{k^2}{\varepsilon} \quad (2.22)$$

### 2.3.2 Model validation

Some validation of the modelling approach is provided in this section relating to a) the pressure drop calculated by the MSA approach (Eq. (2.23)) and b) the mass transfer model which incorporates the combined effects of Henry's and Dalton's Laws, as expressed in Eq. (2.13).

The predicted pressure drop across the absorption column was compared against the experimental data of Strigle [16]. The comparison is presented in Figure 2.5 with the packing factor (Fp), a measure of the resistance to the flow introduced by the packing material, as a parameter. The packing factor of the Raschig rings used for the current study is unknown. Typical packing factors for commercial Raschig rings are listed in Table 2.8. It can be concluded that the resulting pressure drop follows the trend of the experimental data, as it increases as the liquid-to-gas mass ratio is increased. Further, the predicted pressure drop variation is consistent with the experimentally derived curves for packing factors of the order of 1400-1600. As shown in Table 2.8 similarly sized commercial Raschig rings (i.e. having an outer diameter of the order of 8 mm) have packing factors of the same order as that indicated by the computations. This is a further indirect evidence for the accuracy of the computational procedure.

	Title Report on the individual units models	Deliverable number <b>D6.3</b>
		Version <b>3.1</b>

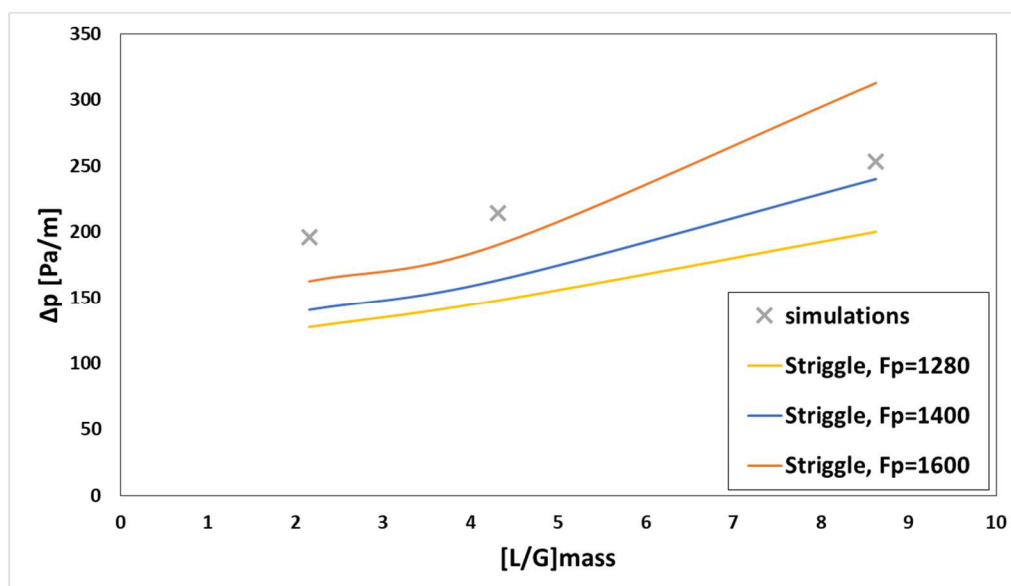


Figure 2.5: Pressure drop variation in the absorption against the experimental data of [16]

Further validation is provided for the mass transfer predictions. Figure 2.6 presents the computed CO<sub>2</sub> solubility in water compared with literature experimental data [17, 18]. The water was used as a solvent for validation for two reasons; a) there is an abundance of well-established data in the literature and b) the CO<sub>2</sub> dissolves in the solvent without reacting, thus the solubility can be independently tested. From the results it can be argued that the simulation follows the trend and the magnitude of the experimental data with a maximum deviation of less than 4% from the data of Dodds et al. [17] and an average relative error of 14% compared to [18].

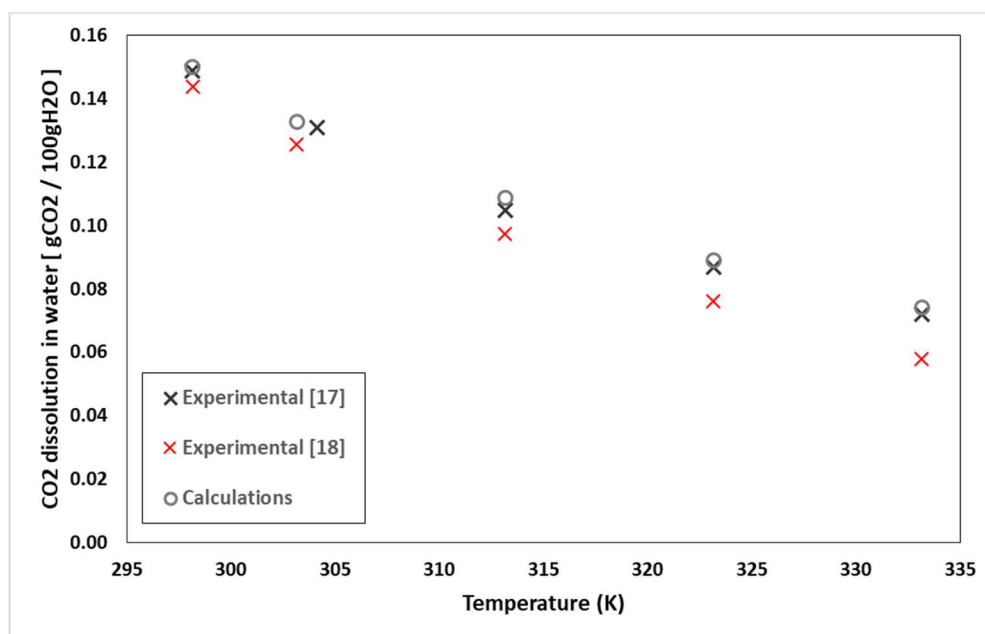


Figure 2.6: Comparison of CO<sub>2</sub> solubility in water with experimental data


	Title Report on the individual units models	Deliverable number <b>D6.3</b>
		Version <b>3.1</b>

Table 2.8: Typical packing factors ( $F_p$ ) of Raschig rings

	Material	Packing Factor ( $F_p$ )	Information
Raschig Ring 1/32" CS, 1/2" OD	Metal	300	Obtained from <a href="https://www.wisconsinstamping.com/">https://www.wisconsinstamping.com/</a>
Raschig Ring 1/32" CS, 1/4" OD	Metal	700	Obtained from <a href="https://www.wisconsinstamping.com/">https://www.wisconsinstamping.com/</a>
Raschig Ring, 3/8" OD	Ceramic	1000	Obtained from <a href="https://checal.com/">https://checal.com/</a>
Raschig Ring, 1/4" OD	Ceramic	1600	Obtained from <a href="https://checal.com/">https://checal.com/</a>
<b>Raschig Ring, 8mm OD</b>	<b>Unknown</b>	<b>Unknown</b>	<b>Packing material of this study</b>

### 2.3.3 Design and operational specifications of the absorption column model

A schematic of the mini plant absorption unit is shown in Figure 2.7. The geometrical and operational characteristics of the mini plant vary according to the IL used and are summarized in Table 2.9.



Figure 2.7: Schematic of the  $\text{CO}_2$  absorption unit

The two-phase flow in the column is modelled as a bubble flow. A bubble flow is characterized by the secondary phase (liquid) forming distributed bubbles throughout the primary phase. The “bubble” diameter is defined by the user and it affects the surface area, the relaxation time and the lift or drag forces i.e. the interaction between the phases. The bubble diameter was set at 2mm, as this is the injection diameter of the experimental process. A schematic of the 2D model is shown in Figure 2.8.


	Title Report on the individual units models	Deliverable number <b>D6.3</b>
		Version <b>3.1</b>

Table 2.9: Operational and design specifications of the pilot scale absorption column in DVGW

	10 wt-% [BDiMIM][Pro] in [BDiMIM][BTA]	[EMIM][OAc]
Pressure (bar)	1 - 1.1	1
Temperature (°C)	80	80
Gas flow rate (L/h)	100-200	150-180
Gas flow composition (v/v)	50 % CO <sub>2</sub> in N <sub>2</sub>	13-33 % CO <sub>2</sub> in N <sub>2</sub>
Solvent flow rate(L/h)	10-40	7-10
Column height (m)	~2	3
Column diameter (m)	0.07	0.07
Packed bed height (m)	1.6 (2 x 0.8 m)	2.4 (3 x 0.8 m)
Packing material	Raschig rings (8 mm)	Raschig rings (8 mm)
Void fraction (-)	Ca. 40%	Ca. 40%

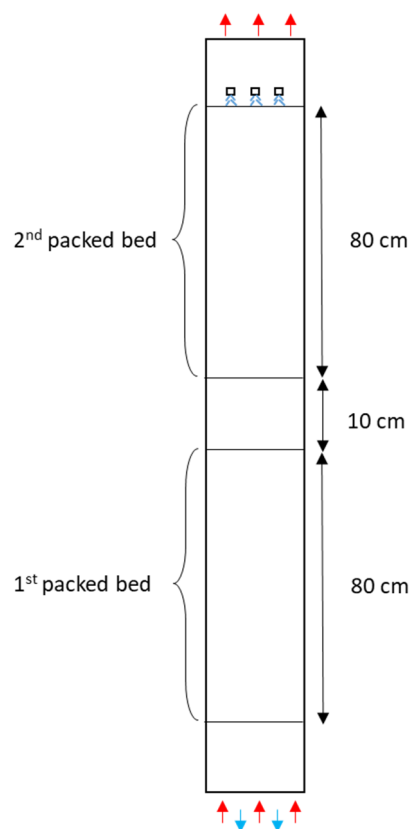



Figure 2.8: Schematic of the 2D model for the absorption process

Flue gases enter the reactor at a temperature of 80 °C from the lower inlet and the solvent is distributed from the top of the column also at a temperature of 80 °C. Note that the solvent and gas temperature are used in CFD simulation is slightly lower than the one used in the ASPEN one i.e. 85 °C to agree the updated operational data from DVGW.

	Title Report on the individual units models	Deliverable number <b>D6.3</b>
		Version <b>3.1</b>

The two identical packed stages, filled with Raschig rings, are placed at the locations shown in Figure 2.8. A simplified injection profile was assumed consisting of three injectors of approximately 0.48 mm diameter each, located immediately above the upper packed bed, while at the same time ensuring that the liquid-to-gas mass flow ratio as well as the gas and solvent superficial velocities match the experimental values. The experimentally determined gas flow rate exits the column from the *column outlet* (the top face) while the *column inlet* (bottom face) was simulated so as to allow both fluids to freely enter and escape the absorption column [19].

There is generally very limited information on mass transfer and chemical reaction processes involving ionic liquids. The two-phase countercurrent flow is modelled macroscopically, which introduces an approximation in the gas-liquid interphase area. Thus, exact representation of the mass transfer would be misleading. In this work, the two-film theory was used to model the mass transfer, in which a negligible gas side mass transfer resistance is a reasonable assumption as the diffusivity of the species in the gas phase is four orders of magnitude higher compared to the ones in the liquid phase. The liquid side mass transfer coefficient is estimated by this study. Mass transfer coefficients of the order of  $10^{-3}$  m/s are used in [19] for carbon dioxide capture by aqueous MEA solution. The dissolution of CO<sub>2</sub> is faster when the reaction kinetics are slower [20]. As the CO<sub>2</sub> reacts substantially slower with an aqueous MEA solution than the corresponding reaction with – the similar IL to our case – 10wt% [BDiMIM][Pro] in [BDiMIM][BTA] mixture (almost an order of magnitude at 40 °C, see Figure 2.9), a lower mass transfer coefficient for the latter case is adopted here.

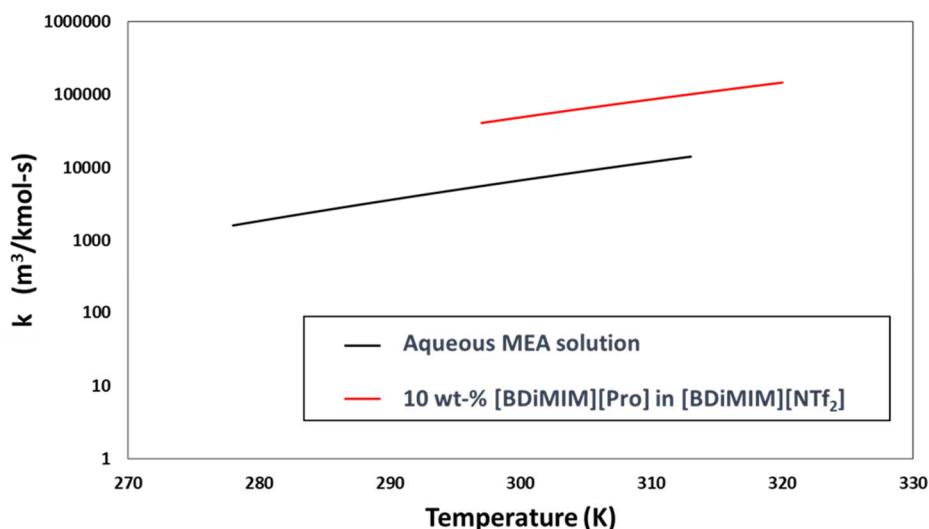
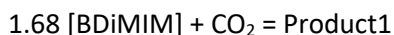



Figure 2.9 Comparison of rate constants for the CO<sub>2</sub> reaction with aqueous MEA [21] and 10 wt-% [BDiMIM][Pro] in [BDiMIM][BTA] [5] as a function of temperature.

The kinetics of CO<sub>2</sub> reaction with the ionic liquids have been obtained from the work of Orloff et al. [5]. The computations presented here relate to the reaction of the 10 wt-% [BDiMIM][Pro] in [BDiMIM][BTA] mixture with carbon dioxide, as shown below



	Title Report on the individual units models	Deliverable number <b>D6.3</b>
		Version <b>3.1</b>

The kinetic parameters used for this reaction are  $E_A = 43830 \text{ J/mol}$  and  $\ln(k_0) = 25.944$ , with  $k$  units being  $\text{m}^3/\text{kmol/s}$  [5] and selected properties of the species involved are presented in the table below.

	[BDiMIM]	CO <sub>2</sub> (l)	CO <sub>2</sub> @85°C	N <sub>2</sub> @85°C	Product1
Density [kg/m <sup>3</sup> ]	1389.3	1.5018	1.5018	0.9532	1389.3
MW [kg/kmol]	407.7	44	44	28.0134	728.9
Viscosity [Pa s]	0.015	0.015	1.778e-05	2.047e-05	0.015
Mass Diffusivity (m <sup>2</sup> /s)	1.2e-9	1.2e-9	1.6e-05	1.6e-05	1.2e-9

### 2.3.4 Simulation results

Typical simulation results are presented in this section. Simulations were performed by assuming a constant flue gas flow rate of 150 L/h and varying the solvent flow rate, as summarized in Table 2.10.

Table 2.10: Details of the four cases examined for the pilot scale absorption column in DVGW shown in Figure 2.10

	Gas flow rate (L/h)	Solvent flow rate (L/h)
<b>Case 1</b>	150	15
<b>Case 2</b>	150	25
<b>Case 3</b>	150	35
<b>Case 4</b>	150	45

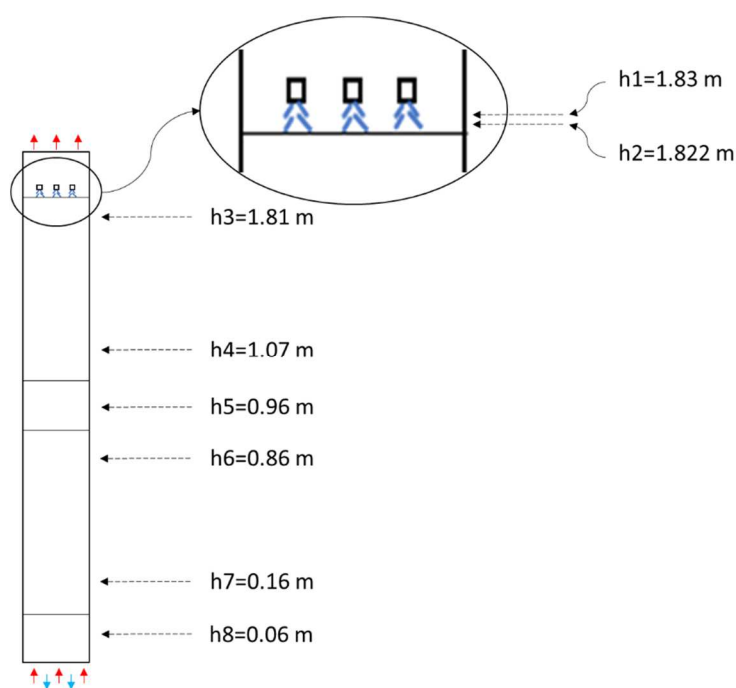



Figure 2.10: Schematic of the eight axial locations chosen for results observation

	Title Report on the individual units models	Deliverable number <b>D6.3</b>
		Version <b>3.1</b>

The radial distribution of solvent velocity and volume fraction are also recorded at eight axial locations at 0.06m (h8), 0.16m (h7), 0.86m (h6), 0.96m (h5), 1.07m (h4), 1.81m (h3), 1.822m (h2) and 1.83m (h1), as indicated in Figure 2.10. These eight locations were selected so as to observe the magnitudes of interest in all key locations i.e. just after the solvent injection inside the upper and lower packed bed and in locations where no packing material exists – after exiting both packing beds.

The variation of the vertical component of the solvent velocity at the selected axial locations for Case 4 is shown in Figure 2.11. Note that the initial injection velocity is 0.16 m/s. The liquid flow initially accelerates and fast decelerates just above the porous zone as the momentum sink induces a pressure drop and the porous zone acts like a porous wall. The actual value of the momentum sink can only be determined experimentally. In the absence of a porous zone no such deceleration is observed. Computations also show that the magnitude of the deceleration is largely independent of the porous zone resistances (see Eq. (2.17) for definitions). Further, velocities at h3 and the h6 locations are exactly equal. After exiting the porous zone the liquid velocity attains an almost uniform parabolic profile.

The radial variation of the solvent volume fraction at the same axial locations is shown in Figure 2.12. Again the volume fractions at h3 and h6 as well as at h4 and h7 coincide. Clearly solvent volume fraction reaches a maximum at the downstream end of the two porous zones as the slowed-down fluid decelerates. The distinct peaks in the porous zone are artificial and are due to the phenomenological description of the flow in the porous zone.

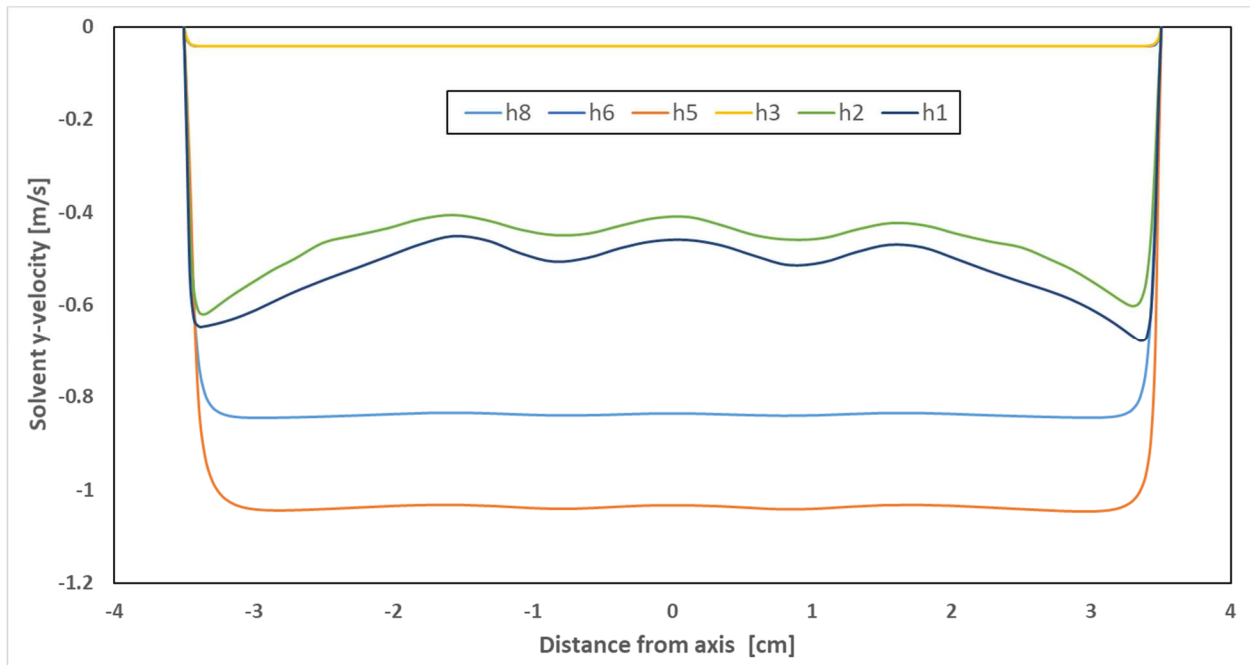



Figure 2.11: Velocity distribution across absorption column at various heights in Case 4



	Title Report on the individual units models	Deliverable number <b>D6.3</b>
		Version <b>3.1</b>

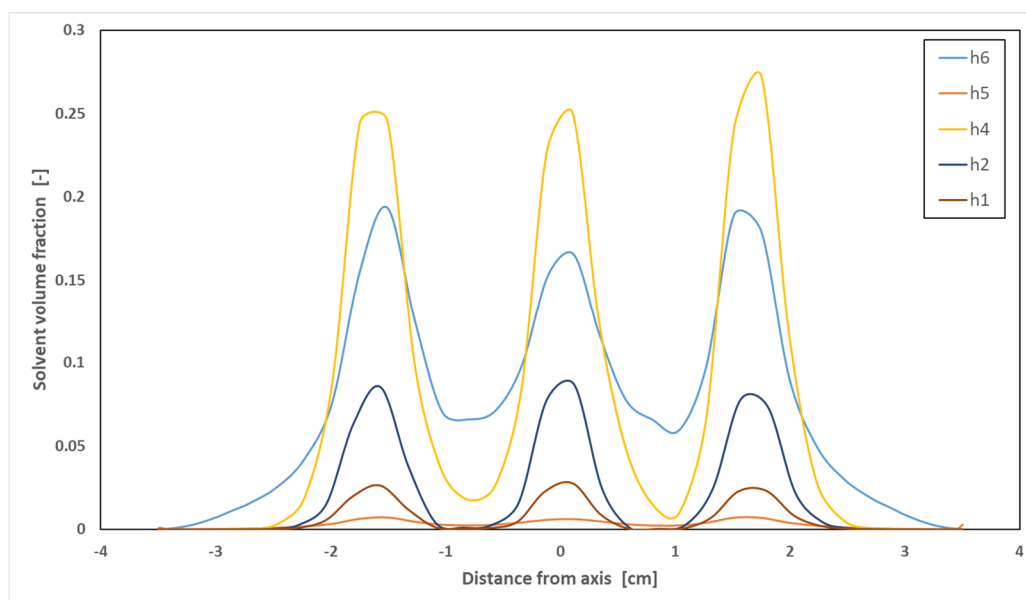


Figure 2.12: Volume fraction distribution across absorption column at various heights in Case 4

CFD calculations can be used to provide crucial design information not accessible with other simulation tools, such as pressure distribution. Figure 2.13 shows the pressure drop along the column for Case 4. There is a monotonic increase of the pressure drop along the column, as expected, and resulting to a total pressure drop of almost 30 Pa or 15 Pa/m. Pressure distribution for all other cases is similar as it is mainly dependent upon the exhaust gas flow. The resulting pressure drop is utilized in the overall system mass and energy balance calculations presented in D6.4.

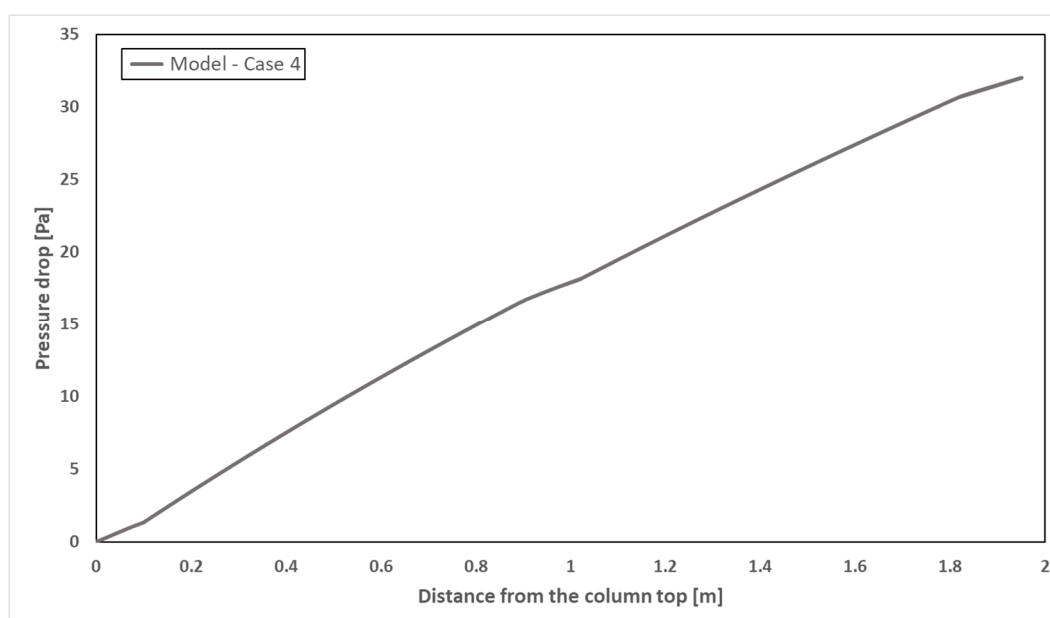



Figure 2.13: Pressure drop along column for Case 4.

	Title <b>Report on the individual units models</b>	Deliverable number <b>D6.3</b>
		Version <b>3.1</b>

The developed model also leads to very accurate predictions of CO<sub>2</sub> levels at the absorber exit and the corresponding column efficiency. Experimental data from the DVGW mini-plant are considered for comparison. The developed model accurately reproduces the substantial decrease in exit CO<sub>2</sub> levels with increasing solvent loading. The level of agreement between computations and experiments is very acceptable although the quality of predictions slightly deteriorates at high solvent loadings. More experimental data are clearly required in order to assess the validity of the model assumptions. Finally, the absorption efficiency can be readily evaluated reaching very acceptable levels (90%) at high solvent flow rates.


#### 2.3.4.1 Conclusions

The work presented in this section provides a detailed CFD description of the multicomponent reacting flow in the absorber column of the CO<sub>2</sub> purification unit. The calculations are performed on the basis of the actual mini plant geometry, the actual operating conditions and the actual solvents used in the DNGW mini plant and described in D3.3. Modelling assumptions have been carefully assessed and the results have been successfully validated against project generated data.

The CFD calculations can serve as to both evaluate a particular design (e.g. regions of intense pressure drop, wall wetting etc.) and predict flow characteristics (e.g. pressure drop across the column, gas and liquid velocity distribution, heat profiles) not accessible through reduced order models that can be used for the design process (e.g. the upscaling of the column in the demo plant). As an example, the detailed CFD simulations provide accurate predictions of global physical and chemical quantities (e.g. pressure drop per column height, CO<sub>2</sub> capture efficiency as a function of gas-to-liquid ratio) that serve as an input in overall system mass and energy balance calculations. This point is discussed further in D6.4.


There are several conclusions to be drawn from the CFD calculations. The flow pattern inside the absorption column is characterized by periodicity induced by the transitional Reynolds number, the coalescence of the issuing bubbles and re-laminarization due to the presence of the porous zone. The interplay of the above phenomena is a strong function both of operating parameters but also of the solvent properties.

The computational methodology outlined in this section is adequate both for describing the local variation of key operating variables (e.g. gas and solvent velocities, pressure distribution, CO<sub>2</sub> concentration) and the extraction of global parameters. However, there is scope for further work mainly related to the more detailed description of the flow patterns inside the packed bed and the extraction of more accurate flow resistance and mass transfer coefficients.


	Title Report on the individual units models	Deliverable number <b>D6.3</b>
		Version <b>3.1</b>

## References

1. Mikulcic, H., Skov, I.R., Dominkovic, D.F., Alwi, A.R.W., Manan, Z.A., Tan, R., Duic, N., Mohamad, S.N.H., Wang, X. Flexible carbon capture and utilization technologies in future energy systems and the utilization pathways of captured CO<sub>2</sub>. *Renew. Sustain. Energy Rev.* 114 (2019) 109338.
2. Luis, P. Use of monoethanolamine (MEA) for CO<sub>2</sub> capture in a global scenario: Consequences and alternatives. *Desalination*, 380 (2016) 93-99.
3. Ramdin, M., de Loos, T.W., Vlucht, T.J. State-of-the-art CO<sub>2</sub> capture with ionic liquids. *Ind. Eng. Chem. Res.* 51 (2012) 8149-8177.
4. Ethanolamines, Form No. 111-01375-0103 AMS. Dow Chemical Company, 2003.
5. Ortloff F., Roschitz, M., Ahrens, M., Graf, F., Schubert, T., Kolb, T. Characterization of functionalized ionic liquids for a new quasi-isothermal chemical biogas upgrading process. *Separation and Purification Technology* 195 (2018) 413-430.
6. Quijada-Maldonado, E., van der Boogaart, S., Lijbers, J.H., Meindersma, G.W., de Haan, A.B. Experimental densities, dynamic viscosities and surface tensions of the ionic liquids series 1-ethyl-3-methylimidazolium acetate and dicyanamide and their binary and ternary mixtures with water and ethanol at T = (298.15 to 343.15 K). *J. Chem. Thermodynamics* 51 (2012) 51-58.
7. Qu, M., Abdelaziz, O., Sun, X-G., Yin, H. Aqueous solution of [EMIM][OAc]: Property formulations for use in air conditioning equipment design. *Appl. Therm. Eng.* 124 (2017) 271-278.
8. Ma, X.-X., Li, L., Wei, J., Duan, W.-B., Guan, W., Yang, J.-Z. Study on enthalpy and molar heat capacity of solution for the ionic liquid [C2mim][OAc] (1-Ethyl-3-methylimidazolium acetate). *J. Chem. Eng. Data* 57 (2012) 3171-3175.
9. Zareiekordshouli, F., Lashanizadehgan, A., Darvishi, P. Study on the use of an imidazolium-based acetate ionic liquid for CO<sub>2</sub> capture from flue gas in absorber/stripper packed columns: Experimental and modeling. *Int. J. Greenh. Gas Control* 70 (2018) 178-192.
10. Aspen Plus User Guide, AspenTech.
11. ANSYS Fluent 16.1
12. Marek, M. Comparison of direct flow simulation in a random packed bed of Raschig rings with a macroscale momentum-sink approach *J. Phys.: Conf. Ser.* 1102 012021, 2018.
13. Andrade, J., Costa, U., Almeida, M., Makse, H., Stanley, H. Inertial effects on fluid flow through disordered porous media. *Phys. Rev. Lett.* 82 (1999) 52495252.
14. Bazmi, M., Hashemabadi, S., Bayat, M. CFD simulation and experimental study of liquid flow mal-distribution through the randomly trickle bed reactors. *Int. J. Heat Mass Transf.* 39 (2012) 736-743.

	Title Report on the individual units models	Deliverable number <b>D6.3</b>
		Version <b>3.1</b>

15. Niegodajew, P., Asendrych D., Amine based CO<sub>2</sub> capture – CFD simulation of absorber performance, Appl. Math. Model. 40 (2016) 10222-10237.
16. Strigle, R.F. Random packings and packed towers: Design and applications. nP, United States, 1987.
17. Dodds, W.S., Stutzman, L.F., Sollami, B.J. Carbon dioxide solubility in water. Ind. Eng. Chem. Chem. Eng. Data Ser. 1 (1856) 92–95. <https://doi.org/10.1021/i460001a018>.
18. Dean, J.A. Physical properties. Solubilities of gases in water. Langes Handb. Chem. 375–380, 1999.
19. Pham, D.A., Lim, Y.-I., Jee, H., Ahn, E., Jung, Y. Porous media Eulerian computational fluid dynamics (CFD) model of amine absorber with structured-packing for CO<sub>2</sub> removal. Chem. Eng. Sci. 132 (2015) 259–270. <https://doi.org/10.1016/j.ces.2015.04.009>.
20. Yokozeki, A., Shiflett, M.B., Junk, C.P., Grieco, L.M., Foo, T. Physical and chemical absorptions of carbon dioxide in room-temperature ionic liquids. J. Phys. Chem. B 112 (2008) 16654–16663. <https://doi.org/10.1021/jp805784u>.
21. Versteeg, G.F., Dijck, L.A.J.V., Swaaij, W.P.M.V. On the kinetics between CO<sub>2</sub> and alkanolamines both in aqueous and non-aqueous solutions. An overview. Chem. Eng. Commun. 144 (1996) 113–158. <https://doi.org/10.1080/00986449608936450>

	Title Report on the individual units models	Deliverable number <b>D6.3</b>
		Version <b>3.1</b>


### 3 CaCO<sub>3</sub> precipitation unit

#### 3.1 Introduction

The second part of the deliverable D6.3 relates to the modelling and simulation of the precipitation/crystallization process. The latter in turns requires an accurate description of the solubility of the electrolytes especially in the presence of other species. Calculation of the solubility of the multicomponent mixture species requires the solution of a set of algebraic equations describing the aqueous electrolyte thermodynamics and interaction between the species, along with reservation equations of total calcium concentration and total alkalinity [1]. Apparently, this set of equations defines the degree of saturation of the species, i.e. the solid phases (if any) of the species of interest. Since the system under investigation includes complexes, intermediates and undissociated aqueous species, as well as a number of species that may precipitate, the calculations are very tedious and time consuming requiring a dedicated software [2]; to this end the Aspen Plus electrolyte module has been assumed to accurately predict the composition of all three phases (gas, liquid, solid) given the temperature, pressure and the initial composition of the aqueous reactive mixture. The integration of the Aspen Plus thermodynamics module into the process modelling environment (gPROMS) is shown in Appendix A invoking the CAPE-OPEN standard.

A parallel step along with the solution thermodynamics is the quantitative analysis and control of key process performance indicators of the kinetics mechanisms and models, which can be supported by dedicated software. Essentially, with the crystallization software modules the theoretical/mechanistic model that has been assumed beforehand is validated against experimental data by systematically estimating the parameters; for instance, the initial assumptions of the crystallization mechanisms (e.g. primary/secondary nucleation, growth and dissolution etc.) can be further screened so that the dominant mechanisms are applied. The latter can be also supported by qualitative discrimination the active mechanisms, e.g. SEM images would reveal whether agglomeration is negligible. Sensitivity analysis and the updated mechanisms with respect to process parameters can lead to more efficient model-based scale-up and technical transfer of the crystallizer.

The last step is the integration of all these phenomena and their adaptation to the process considered, that of the membrane module. The crucial factor is the presence of the membrane in order to separate the gas and the liquid flows, but also to provide an enhanced mass transfer area for the components transport through the membrane to take place. The identification of the suitable membrane structure and the quantifiable characteristics of the membrane material itself, such as tortuosity, porosity and range of pore sizes, as provided by the commercial membrane modules manufacturer and found in the literature when unavailable, is in progress. These values determine the effective diffusive fluxes through the membrane pores, which take into account Knudsen and molecular diffusion. The membrane modules promoted so far through WP4 comprise a hybrid approach for mass transfer and reaction, while providing much enhanced mass transfer area (known a priori) and pore size which influence the crystals production. The prediction of the final production distribution stems from the detailed description of the nucleation and growth rates of the particles; the interaction between liquid and gas phases in terms of appropriate

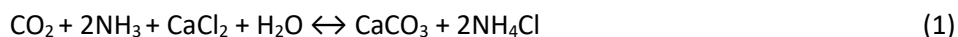
	Title Report on the individual units models	Deliverable number <b>D6.3</b>
		Version <b>3.1</b>

mass transfer coefficients, reaction rates and physicochemical properties. In the following lines the main individual steps are analysed and modelled.

### 3.2 Aqueous electrolyte thermodynamics

Following Al-Malah [3], an electrolyte system is made up of chemical species that can dissociate partially or totally into ions in a solvent. The liquid phase reaction always occurs under equilibrium conditions between the condensed state and the dissociate form, while the presence of the latter requires non-ideal solution thermodynamics, that is, activity coefficients taking values other than unity. It is convenient to use a dedicated software/method for electrolyte systems, such as ELECNRTL for Aspen Plus®, when rigorous modelling of electrolyte species is required. Aspen Plus has a large built-in databank of electrolyte reactions and interaction parameters for many electrolyte systems. The Aspen Plus Electrolytes Wizard generates electrolytes chemistry automatically and interactively, so one can control the species and reactions to include in the simulation [4].

For the general reaction:



there are multiple secondary reactions involving ions, which are summarized in Table 3-1. Use of  $\text{H}_3\text{O}^+$  (instead of  $\text{H}^+$ ) is strongly recommended by Aspen Plus, because the presence of  $\text{H}_3\text{O}^+$  in the solution chemistry is better able to represent the phase and chemical equilibrium of almost all electrolyte systems [4]. The ELECNRTL module makes extended use of the Aspen Plus reactions database, from which the (optional) equilibrium constant coefficients are automatically retrieved. The general expression for calculating the equilibrium constants is:


$$\ln(K_{eq}) = A + \frac{B}{T} + C \ln(T) + D \cdot T \quad (2)$$

where  $K_{eq}$  is the equilibrium constant and  $T$  the temperature (in °C).

Table 3-1 summarizes the equilibrium constant coefficients. When not present, Aspen Plus will calculate the chemical equilibrium from the Gibbs free energy of the participating components [4]. Apart from the equilibrium constant parameters, Aspen Plus requires a multitude of other parameters, such as the binary interaction Henry's Law parameters and the binary interaction VLCLK (Clarke density) parameters, which are given in Table 3-3. For further details about the ELECNRTL model and its assumptions the reader is referenced to [3-7].

Table 3-1. Aspen Plus notation of the overall reactions scheme using the ELECNRTL module.

#	Reaction Type	Reaction
1	Equilibrium	$\text{HCL} + \text{H}_2\text{O} \leftrightarrow \text{CL}^- + \text{H}_3\text{O}^+$
2	Equilibrium	$\text{NH}_3 + \text{HCO}_3^- \leftrightarrow \text{H}_2\text{O} + \text{NH}_2\text{COO}^-$
3	Equilibrium	$\text{NH}_3 + \text{H}_2\text{O} \leftrightarrow \text{OH}^- + \text{NH}_4^+$
4	Equilibrium	$\text{HCO}_3^- \leftrightarrow \text{CO}_3^{--} + \text{H}^+$
5	Equilibrium	$2 \text{H}_2\text{O} + \text{CO}_2 \leftrightarrow \text{HCO}_3^- + \text{H}_3\text{O}^+$
6	Equilibrium	$\text{CAOH}^+ \leftrightarrow \text{CA}^{++} + \text{OH}^-$
7	Equilibrium	$2 \text{H}_2\text{O} \leftrightarrow \text{OH}^- + \text{H}_3\text{O}^+$
CALCI(S)	Salt	$\text{CALCI}(\text{S}) \leftrightarrow \text{CAOH}^+ + \text{OH}^-$

	Title Report on the individual units models	Deliverable number <b>D6.3</b>
		Version <b>3.1</b>

CACO3(S)	Salt	CACO3(S) <--> CO3-- + CA++
AMMON(S)	Salt	AMMON(S) <--> HCO3- + NH4+
NH4CL(S)	Salt	NH4CL(S) <--> CL- + NH4+
SALT4	Salt[4]	CACL2.2H2O <--> CA++ + 2 H2O + 2 CL-
SALT3	Salt[3]	CACL2.4H2O <--> CA++ + 2 CL- + 4 H2O
SALT2	Salt[2]	CACL2.6H2O <--> CA++ + 2 CL- + 6 H2O
SALT1	Salt[1]	CACL2.H2O <--> H2O + CA++ + 2 CL-
CACL2(S)	Salt	CACL2(S) <--> CA++ + 2 CL-
CACL2	Dissociation	CACL2 --> CA++ + 2 CL-


Table 3-2. Equilibrium constant coefficients used by Aspen Plus.

Reaction	A	B	C	D
1*	-	-	-	-
2	-4.58344	2900	0	0
3	-1.25656	-3335.7	1.4971	-0.03706
4	216.05	-12431.7	-35.4819	0
5	231.465	-12092.1	-36.7816	0
6*	-	-	-	-
7	132.889	-13445.9	-22.4773	0
CALCI(S)*	-	-	-	-
CACO3(S)*	-	-	-	-
AMMON(S)	554.818	-22442.5	-89.0064	0.064732
NH4CL(S)	-141.676	-880.103	27.7806	-0.06317
SALT4	-1504.26	44596	257.013	-0.376
SALT3	42.3592	0	-10.9919	0.049194
SALT2	1397.39	-31788.4	-255.455	0.526739
SALT1	5.95216	0	0	-0.01806
CACL2(S)*	-	-	-	-

\*Calculated by the Gibbs free energy expressions

Table 3-3. Henry's Law and VLCLK (Clarke density) parameters used by Aspen Plus.

Henry's Law parameters			
Component i	NH <sub>3</sub>	CO <sub>2</sub>	HCl
Component j	H <sub>2</sub> O	H <sub>2</sub> O	H <sub>2</sub> O
A <sub>ij</sub>	-144.976	159.2	46.94
B <sub>ij</sub>	-157.552	-8477.71	-7762.83
C <sub>ij</sub>	28.1001	-21.9574	0
D <sub>ij</sub>	-0.04923	0.005781	0
T <sub>low</sub> (°C)	-0.15	-0.15	-0.15
T <sub>upper</sub> (°C)	224.85	226.85	126.85
Clarke density parameters			
Component i	H <sub>3</sub> O+	NH <sub>4</sub> +	
Component j	Cl-	Cl-	
VCA	34.5511	41.2177	
ACA	13.3658	-12.3551	

	Title Report on the individual units models	Deliverable number <b>D6.3</b>
		Version <b>3.1</b>

### 3.3 Membrane crystallization technology

Membrane-based gas absorption and reaction are gaining attention as an alternative to industrially well-established gas separation and reaction equipment, such as reactive absorption columns, because of membrane modules' high mass transfer area (known a priori), modular design, easy scale-up [8-9] and straightforward modelling of their flow behaviour [10]. Membrane-assisted crystallization operates in a well-controlled manner, thus it can master crystallization by modulating system conditions and even the physico-chemical properties of the membranes [11].

The gas-liquid contact membrane process considers a mixture (gas or liquid) flowing in the lumen (fiber side), which is confined by the presence of the membrane not allowing direct contact of the mixture (liquid or gas) flowing in the outer part of the membrane, in the shell side. For this type of process the membrane itself does not introduce any selectivity to one gas species over the other: the extent of the separation of the mixture depends on the solubility difference of the species into the selected shell-side liquid solvent [12], and especially on whether gas-liquid reactions take place.

Hollow fiber membrane processes have been mainly described by mathematical models involving concentration gradients within the fiber by solving the mass continuity equation [13]. In principle, efforts have been focused on heat transfer models in laminar flow in various geometries, which later were extended to postulate the mass-conservation equation, accounting also for various boundary conditions in terms of Nusselt numbers for the case of heat transfer [14-15], or Sherwood numbers for mass transfer [10, 16].

The overall model has been extensively described by Pantoleontos et al. [10, 17], and it is briefly mentioned here with additional details for convenience. The following assumptions are made to describe the fluid flow within the fiber and the transport of the diffusing component through the membrane pores: (a) under steady state and isothermal operation; (b) Newtonian fluids physical properties; (c) fully developed, laminar flow in the lumen (fiber); (d) applicability of Henry's law; (e) when the velocity profile is fully developed, velocity term in radial direction becomes zero; (f) axial molecular diffusion can be neglected compared to axial convection, when the Peclet number is greater than 100.

Considering the assumptions above continuity equation in a fiber (lumen side) becomes:

$$2 \cdot u \left[ 1 - \left( \frac{r}{R_f} \right)^2 \right] \frac{\partial C}{\partial z} = D \left[ \frac{1}{r} \frac{\partial}{\partial r} \left( r \frac{\partial}{\partial r} \right) \right] \quad (3)$$

$$\text{with the associated boundary conditions (see also Fig. 1): } C(z=0, r) = C_0 \quad (4)$$

$$\frac{\partial C}{\partial r}_{z,r=0} = 0 \quad (5)$$

(symmetry boundary condition at the fiber center)

$$D \frac{\partial C}{\partial r}_{z,r=R} = -K_{ext} [C(z, r = R_f) - mC_s] \quad (6)$$



	Title Report on the individual units models	Deliverable number <b>D6.3</b>
		Version <b>3.1</b>

where  $u$  is the average velocity in the lumen,  $C$  is the concentration of the diffusing component,  $C_0$  is the initial concentration,  $D$  is the diffusion coefficient of the diffusing component, and  $R$  is the reactive source term if the reaction takes place in the lumen side (otherwise, this term is zero).

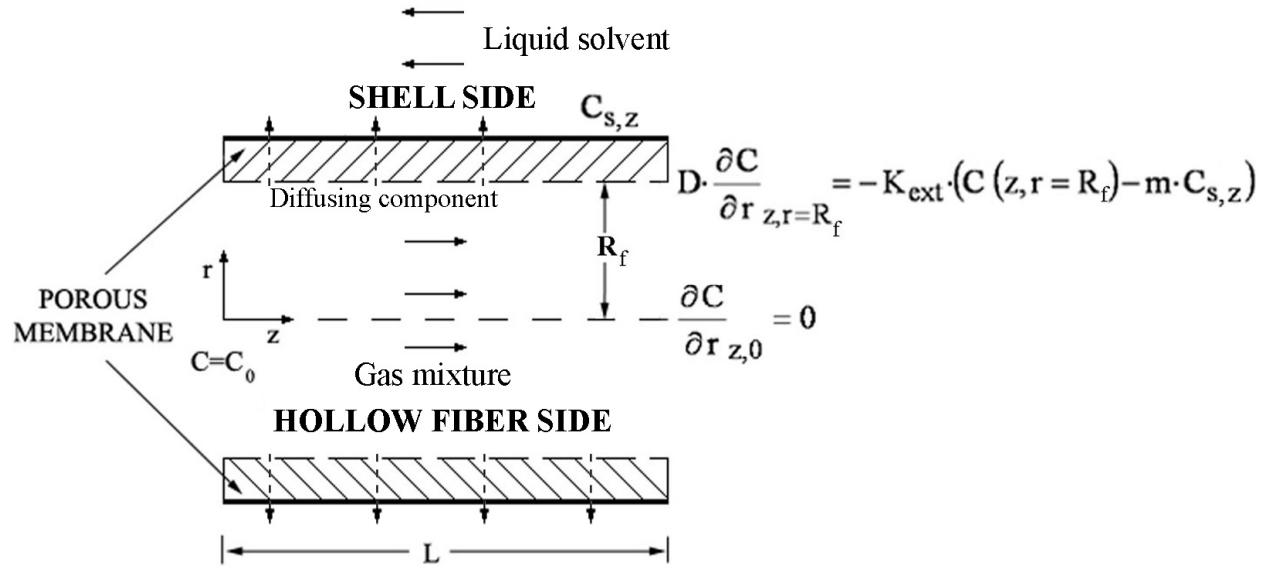


Figure 3-1. A single hollow fiber flow pattern with gaseous mixture flowing in the lumen-side and counter-current mode of operation depicting the corresponding boundary conditions (adapted from [17]).


The term  $m$  is the equilibrium coefficient of the diffusing component corresponding to equilibrium conditions between the lumen and shell fluids depending on the physical properties of the fluids [10, 17], e.g. it is related to the dimensionless Henry's constant in gas-liquid contact membrane systems [18], or to the partition coefficient in membrane-based extraction [19]. Apart from the absorbed  $\text{CO}_2$  in water, there is mainly the general reaction (1), which augments the driving force between lumen and shell side enhancing mass transfer and removal of  $\text{CO}_2$ . The extent of combining physical absorption and chemical reaction of  $\text{CO}_2$  with the reacting solvent is largely unknown, and can be inferred by comparing experimental data with the computational model's results. In the same manner as the physical absorption expressions, e.g.  $\text{CO}_2$  absorbed in water, the enhanced (including reaction) removal of  $\text{CO}_2$ , is accounted for by the incorporation of an enhancement factor,  $E$ . The term,  $m$  (no units), is then given by:

$$m = \frac{E}{H_{\text{CO}_2}RT} \quad (7)$$

where  $R$  is the gas constant and  $H_{\text{CO}_2}$  is the Henry's constant of  $\text{CO}_2$  in water, that is, if only physical absorption takes place, and it is given by [20]:

$$H_{\text{CO}_2} = 3.54 \cdot 10^{-8} e^{\frac{2044}{T}} \text{ mol/cm}^3/\text{bar} \quad (8)$$

For a case in which the gaseous mixture flows in the lumen and the species of interest diffuses through the membrane pores and reacts with the liquid bulk phase in the shell-side, the overall mass transfer coefficient,  $K_{\text{ext}}$ , includes all relevant mass transfer resistances and layers of transport between the membrane and the shell-side boundary layer: the membrane itself, including any partial wetting imposed

	Title <b>Report on the individual units models</b>	Deliverable number <b>D6.3</b>
		Version <b>3.1</b>

by the penetrating liquid into the membrane pores, and the shell-side diffusion boundary layer including any enhancement factor because of the reactive mixture:

$$\frac{1}{K_{ext}} = R_m + R_s \quad (9)$$

where  $R_m$  and  $R_s$  are the membrane and the shell-side mass transfer resistances, respectively.

Figure 3-1 shows where each boundary condition is located. The term  $C_{s,z}$  is the concentration of the diffusing component in the solvent, and it is generally assumed varying with  $z$ -direction in the shell side (Case B) depending mainly on the solvent shell-side flow-rate: if the latter is high, then  $C_{s,z}$  variation can be assumed to be negligible (and  $C_{s,z}$  to be constant – Case A); thus, Case A is a sub-case of Case B. The right-hand side (RHS) of Equation (6) is the sink term of mass transfer within a hollow fiber; if it is zero the fiber is said to be insulated (in an adiabatic heat-transfer-like behaviour), and no diffusion occurs through the membrane pores. Equation (6) is reduced to a Dirichlet-type BC (Lévéque-Graetz BC) when the combined mass transfer coefficient,  $K_{ext}$ , is very large [10, 17-21], a case presenting no practical interest, since no membrane mass transfer resistance is assumed whatsoever.

Mini-modules are increasingly gaining attention and they were used in a number of cases [9]. In this study a Liqui-Cel MiniModule 1 x 5.5 is used as a gas-liquid contactor whose characteristics are listed in Table 3-4. These data are used for the simulation of the membrane-based crystallization; additional equations and the method of solution is presented in Appendix B.

*Table 3-4. Gas-liquid membrane contactor.*


Cartridge configuration	Parallel flow
Maximum flow rates	500 ml/min
Effective length	10 cm
Membrane material	Polypropylene
Membrane porosity	40 %
OD / ID	300 $\mu$ m OD / 220 $\mu$ m ID
Number of fibers	2300
Active surface area ( $A_m$ )	0.18 m <sup>2</sup>

### 3.4 Results & Discussion

The experimental procedure examines CO<sub>2</sub> absorption and reaction according to the general reaction scheme (1), when the reactive solvent (aqueous solution of 885 mM CaCl<sub>2</sub>, 19.5 mM NH<sub>4</sub>OH)<sup>1</sup> flows in the shell-side and the gas mixture containing 20 % CO<sub>2</sub> – 80 % N<sub>2</sub> flows co-currently in the lumen-side. Gas flowrates were varied from 270 to 1400 cm<sup>3</sup>/min and the liquid flowrates from 165 to 440 cm<sup>3</sup>/min. Experiments were carried out at ambient conditions and the molar fractions of CO<sub>2</sub> were measured at the inlet (lumen entrance) and exit (lumen outlet).

In order to derive the enhanced CO<sub>2</sub> Henry's constant and the overall mass transfer coefficient presented in Eqs. (7) and (9), the set of Equations (13), (18)-(19) is solved. For co-current mode of operation by

<sup>1</sup> mM = 10<sup>-3</sup> M = 10<sup>-3</sup> mol/L

	Title Report on the individual units models	Deliverable number <b>D6.3</b>
		Version <b>3.1</b>


counting from the entrance of the lumen (that is,  $z=0$ ),  $C_s^* = C_{s,0} = 0$  (the reactive solvent enters co-currently with no  $\text{CO}_2$  dissolved).

The removal efficiency increases with the increase of the liquid flowrate (alternatively: when liquid flowrate remains constant and gas flowrate decreases) as higher amounts of liquid solvent are available to absorb and react with the gas flowing in the lumen. The highest removal of  $\text{CO}_2$  was 0.8326, which has a near-unity liquid-to-gas flowrate ratio.

The results of the parameter-estimation procedure were obtained using the built-in Optimisation module of gPROMS. First of all, it is seen that the highest mass transfer coefficient value (and consequently, the  $Sh_w$ ) is derived from the experiment with the least removal. This is in accordance with observations made by Pantoleontos et al. (2017) when using the same model (Case B) with a physical-absorption case [17]. It is concluded by the model that the mass transfer coefficient is positively correlated with the  $m^*$  parameter: for higher  $m^*$  values implying increased values of  $Q_g$  or decreasing values of  $Q_l$  (or both) the trans-membrane flux is higher due to the higher amount of lumen fluid compared to shell-side solvent amounts. However, as smaller amounts of liquid are available to absorb and react with the diffusing gas through the membrane pores, the overall removal of the gas of interest is smaller. Another observation is the small values of  $Sh_w$ , which are comparable with a physical absorption case (see e.g. [17]) due to the co-current mode of operation and the mini-module utilized in the current study. Still, the removal efficiency is much greater owing to the enhancement factor introduced by the reactive conditions of the general reaction (1).

The degree of  $\text{CO}_2$  removal was calculated by experimental results and Eq. (19) and compared with the enhancement factor calculated by the model. It is seen that there is an almost linear relation between  $\text{CO}_2$  removal and  $E$ . Obviously, as the removal increases the parameter-estimation (optimization) procedure is directed to increased values of the enhancement factor in order to match the experimental data. In any case, more experimental data could be arranged in order to have a complete picture of the correlations between  $m^*$ ,  $E$ , and  $K_{ext}$  (e.g. by retaining the same  $z^*$  value (that is, the same  $Q_g$ ) and altering only the  $Q_l$ ).

Figure 3-4 shows lumen-side dimensionless  $\text{CO}_2$  concentration ( $C^*$ ) with respect to  $r^*$  and  $z^*$ . The main concentration variation naturally occurs along  $z^*$  compared to  $r^*$  due to the higher  $z$ -length ( $10^{-1}$  m) compared to the very small fiber radius ( $11 \times 10^{-5}$  m) and the small values of  $Sh_w$ , which would otherwise – for higher  $Sh_w$  values – give a steeper concentration profile also in the  $r$ -direction. However, there is  $r$ -variation that cannot be neglected, especially near  $r^*=1$ , where the concentration gradient (sink-term) is dominant. The resemblance of an 1-D behaviour in the lumen side does not entail that a 2-D formulation is unnecessary, since the former requires the transformation of the flux-term (Eq. (6) into a flux-difference term to be incorporated into the mass-conservation (now as an 1-D) Eq. (3).

	Title Report on the individual units models	Deliverable number <b>D6.3</b>
		Version <b>3.1</b>

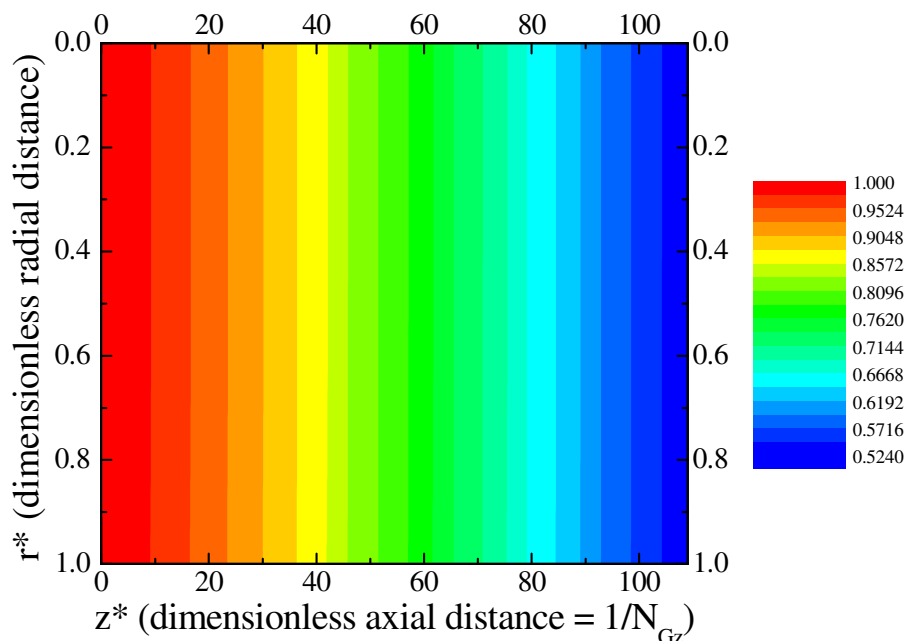


Figure 3-4. Contour plot of lumen-side dimensionless CO<sub>2</sub> concentration for experiment No. 5.


Figures 3-5 and 3-6 depict the CO<sub>2</sub> shell-side concentration for all experiments conducted as predicted by the simulation procedure. This concentration amounts for all CO<sub>2</sub>-related species present in the shell-side, that is, CO<sub>2</sub> dissolved in water (CO<sub>3</sub><sup>2-</sup> and HCO<sub>3</sub><sup>-</sup>; see Table 1), or CO<sub>2</sub> having reacted (CaCO<sub>3</sub>), or even CO<sub>2</sub> in gaseous form (neither reacted or dissolved). The information of the CO<sub>2</sub>-related species composition is given by aqueous electrolyte thermodynamics as derived by the ELECNRTL module of Aspen Plus incorporated into gPROMS calculation procedure via the CAPE-OPEN standard.

Table 3-7 summarizes the species concentrations at the shell-side outlet for one experiment pass as calculated by Aspen Plus. For the operating conditions and initial composition of the reacting mixture it can be seen that there is still NH<sub>3</sub> present at the shell-side not having reacted. The main CO<sub>2</sub>-related species is CaCO<sub>3</sub> accounting for over 99.98% of all CO<sub>2</sub>-related species, while the second-in-order CO<sub>3</sub><sup>2-</sup> species accounts for 0.0127%. Thus, it may be concluded that the CO<sub>2</sub> concentration depicted in Figs. 3-5 and 3-6 for all experiments is also the variation of CaCO<sub>3</sub> in the shell-side over  $z^*$ .

Due to the co-current mode of operation the shell-side concentration of the diffusing species is zero at  $z^*=0$  (the reactive solvent enters at  $z^*=0$  with no CO<sub>2</sub> dissolved). Thus, the CaCO<sub>3</sub> concentration increases along the shell-side length showing the highest gradient (roughly speaking this gradient is derived by  $\left| \frac{\Delta C_{S,z}}{\Delta z^*} \right|$ ) near  $z^*=0$ , where the concentration difference between the lumen and the shell-side (accounting for the  $m^*$  parameter) is the highest.

Table 3-7. Species shell-side concentration at the outlet of the module for experiment No. 2 as predicted by Aspen Plus.

Species	Outlet shell-side concentration (moles/cm <sup>3</sup> )	Species	Outlet shell-side concentration (moles/cm <sup>3</sup> )
CaCl <sub>2</sub>	-	CaCl <sub>2</sub> (S)	-
NH <sub>3</sub>	8.79x10 <sup>-04</sup>	SALT1	-

	Title Report on the individual units models	Deliverable number <b>D6.3</b>
		Version <b>3.1</b>

CO <sub>2</sub>	1.86x10 <sup>-15</sup>	SALT2	-
CA++	1.24x10 <sup>-05</sup>	SALT3	-
CAOH+	2.56x10 <sup>-07</sup>	SALT4	-
H <sub>3</sub> O+	7.22x10 <sup>-15</sup>	NH <sub>2</sub> COO-	3.24x10 <sup>-10</sup>
NH <sub>4</sub> +	1.57x10 <sup>-05</sup>	HCO <sub>3</sub> -	1.16x10 <sup>-10</sup>
CACO <sub>3</sub> (S)	7.09x10 <sup>-06</sup>	OH-	1.23x10 <sup>-06</sup>
NH <sub>4</sub> CL(S)	-	CL-	3.95x10 <sup>-05</sup>
AMMON(S)	-	CO <sub>3</sub> --	9.03x10 <sup>-10</sup>
CALCI(S)	-		

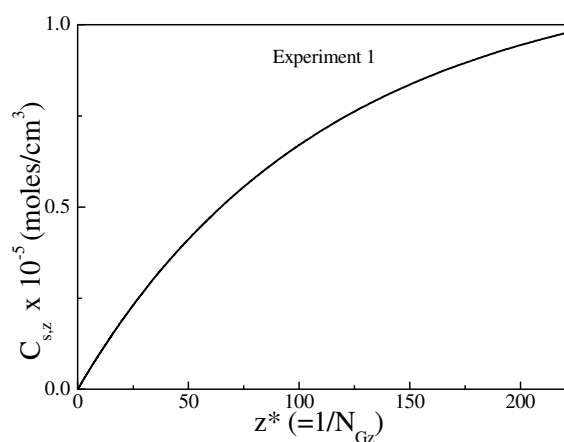


Figure 3-5. Shell-side concentration of CO<sub>2</sub> with respect to z\* for experiment No. 1.

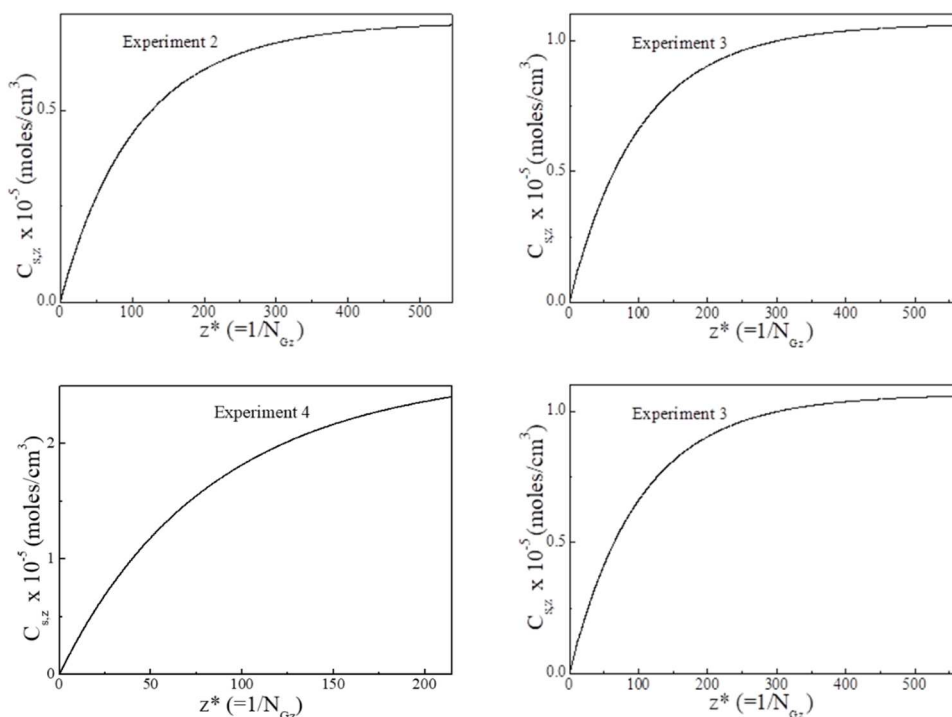



Figure 3-6. Shell-side concentration of CO<sub>2</sub> with respect to z\* for experiments No. 2-5.

	Title Report on the individual units models	Deliverable number <b>D6.3</b>
		Version <b>3.1</b>

### 3.5 Conclusions & Outlook


This study aims to postulate the behaviour of a gas-liquid contact membrane process by describing fully developed, laminar flow under steady state conditions in the lumen-side incorporating shell-side concentration variation equations. This model is tested with the aid of a reactive absorption case, which consists of a gas mixture of  $\text{CO}_2\text{-N}_2$  flowing in the lumen, from which  $\text{CO}_2$  is separated by diffusion into aqueous solution of  $\text{CaCl}_2$  and  $\text{NH}_4\text{OH}$  which flows in the shell side. The model also accounts for process conditions, fluids properties for chemical absorption case, and module geometric characteristics.

The unknown parameters of the overall mass transfer and the enhancement factor due to reactive absorption are also calculated by comparing the experimental data with the postulated model. It is revealed that the highest predicted mass transfer coefficient value (and consequently, the  $\text{Sh}_w$ ) develops in the experiment with the least removal in accordance with previous literature observations. The  $\text{Sh}_w$  values can be directly linked to scaled-up cases where the  $N_{\text{Gr}}$  and  $m^*$  values are comparable, when a membrane module with the same configuration (e.g. co-current mode, parallel flow) is used.

Furthermore, a pattern may be discerned indicating a correlation of an increasing overall mass transfer coefficient with an increasing  $m^*$  value due to increased values of  $Q_g$  or decreasing values of  $Q_l$  (or both). Additionally, it is seen that there is an almost linear relation between  $\text{CO}_2$  removal and enhancement factor, because the parameter-estimation (optimization) procedure is directed to increased values of the enhancement factor in order to match the experimental data. In any case, more experimental data could be arranged in order to have a complete picture of the correlations between  $m^*$ ,  $E$ , and  $K_{\text{ext}}$ .

Aqueous electrolyte thermodynamics is incorporated in the process modelling environment using the Aspen Plus ELECNRTL module for the thermodynamics calculation in combination with the gPROMS equation based software for the process simulation and optimization taking advantage of the CAPE-OPEN standard. Aspen Plus calculations reveal that for the operating conditions and initial composition of the reactive mixture examined the major  $\text{CO}_2$ -related product is  $\text{CaCO}_3$  accounting for almost 100% of the  $\text{CO}_2$ -related species, which allows for the variation calculation of the  $\text{CaCO}_3$  production along the shell-side length of the membrane module.

Results obtained in this section are utilized in the overall system mass and energy balances presented in D6.4.

	Title Report on the individual units models	Deliverable number <b>D6.3</b>
		Version <b>3.1</b>

## Appendix A - Coupling of Aspen Plus and gPROMS: the CAPE-OPEN standard

The CAPE-OPEN standard defines rules and interfaces that allow CAPE (Computer-Aided Process Engineering) applications or components to interoperate. A number of commercial simulation software packages are available to support process modelling providing an environment which allows a process flowsheet to be constructed and the process fluid thermodynamics to be incorporated. “The CAPE-OPEN project formally identified such a modelling programme as a Process Modelling Environment (PME) with the requirement that users of a PME should be able to easily connect the PME with other modelling tools without the need to develop bespoke interfaces”. In the current study gPROMS serves as the PME, which draws the physical and thermodynamic properties data from Aspen Plus via a .cota file generated in the latter and called whenever needed by the former. Successful linking of ASPEN and gPROMS via the CAPE-OPEN standard has been also reported in the literature (see e.g. the most recent [22-27]).

### Flash calculation example


Once the ELECNRTL module is exported from Aspen Plus containing all relevant information (detailed reactions scheme – see Table 3-1 – with all relevant data – see Tables 3-2 and 3-3) it can be invoked from gPROMS via the TPFlash(T, P, n) command – method corresponding to CAPE-OPEN flash calculations – which returns the equilibrium temperature and pressure, and the vector of the species composition in all phases. In the following example no flow-mode has been assumed; only flash calculation is performed given initial temperature and pressure, as well as molar composition of an initial mixture of H<sub>2</sub>O, CaCl<sub>2</sub>, NH<sub>3</sub> and CO<sub>2</sub>. The example examines whether addition of CO<sub>2</sub> results to increased production of CaCO<sub>3</sub>, as well as pH measurements and CO<sub>2</sub>-related ion species for a range of initial CO<sub>2</sub> molar amount. The initial molar flowrates of the relevant components are given in Table 3-8.

*Table 3-8. Operating conditions and range of molar flowrates for the reactive mixture.*

T (°C)	P (atm)	F <sub>H2O</sub> (kmol/h)	F <sub>CaCl2</sub> (kmol/h)	F <sub>NH3</sub> (kmol/h)	Range of F <sub>CO2</sub> (kmol/h)
20	1	110.64	0.03	3.78	0.005-3.64

Ultimately the process deals with the production of 3 kg/h of CaCO<sub>3</sub>, which is the goal of the final pilot-plant production. Figure 3-7 depicts the evolution of pH, ion species concentration (carbonate and bicarbonate, CO<sub>3</sub><sup>2-</sup> and HCO<sub>3</sub><sup>-</sup>), production of CaCO<sub>3</sub>, and any unreacted CO<sub>2</sub>. This figure is broken down to two initial CO<sub>2</sub> molar fraction (y<sub>CO2</sub>) ranges for better visibility, namely the ranges {0.00005-0.03} and {0.03-0.03082}. It is seen that production of CaCO<sub>3</sub> increases up to 3.048 kg/h at y<sub>CO2</sub> equal to 0.000933: this is actually the global maximum of CaCO<sub>3</sub> production. Above the aforementioned CO<sub>2</sub> molar fraction no more CaCO<sub>3</sub> is produced, thus CO<sub>2</sub> is subsequently “physically” absorbed in water.

Above the value of y<sub>CO2</sub> = 0.000933 any added CO<sub>2</sub> to the initial mixture up to y<sub>CO2</sub> = 0.03 results to dissociation of CO<sub>2</sub> in water into the relevant carbonate (CO<sub>3</sub><sup>2-</sup>) and bicarbonate (and HCO<sub>3</sub><sup>-</sup>) species. The amount of both species keeps increasing until y<sub>CO2</sub> = 0.01 with CO<sub>2</sub> further dissociating into water. The bicarbonate species is substantially higher than that of the carbonate species due to equilibrium reaction

	Title Report on the individual units models	Deliverable number <b>D6.3</b>
		Version <b>3.1</b>

5 (see Table 1) at the expense of water. From  $y_{\text{CO}_2} = 0.03$  any added  $\text{CO}_2$  amount cannot dissociate further as the system becomes saturated: the amounts of all  $\text{CO}_2$ -related ion species become steady and the  $\text{CO}_2$  amount in excess exits the process as unreacted gas.

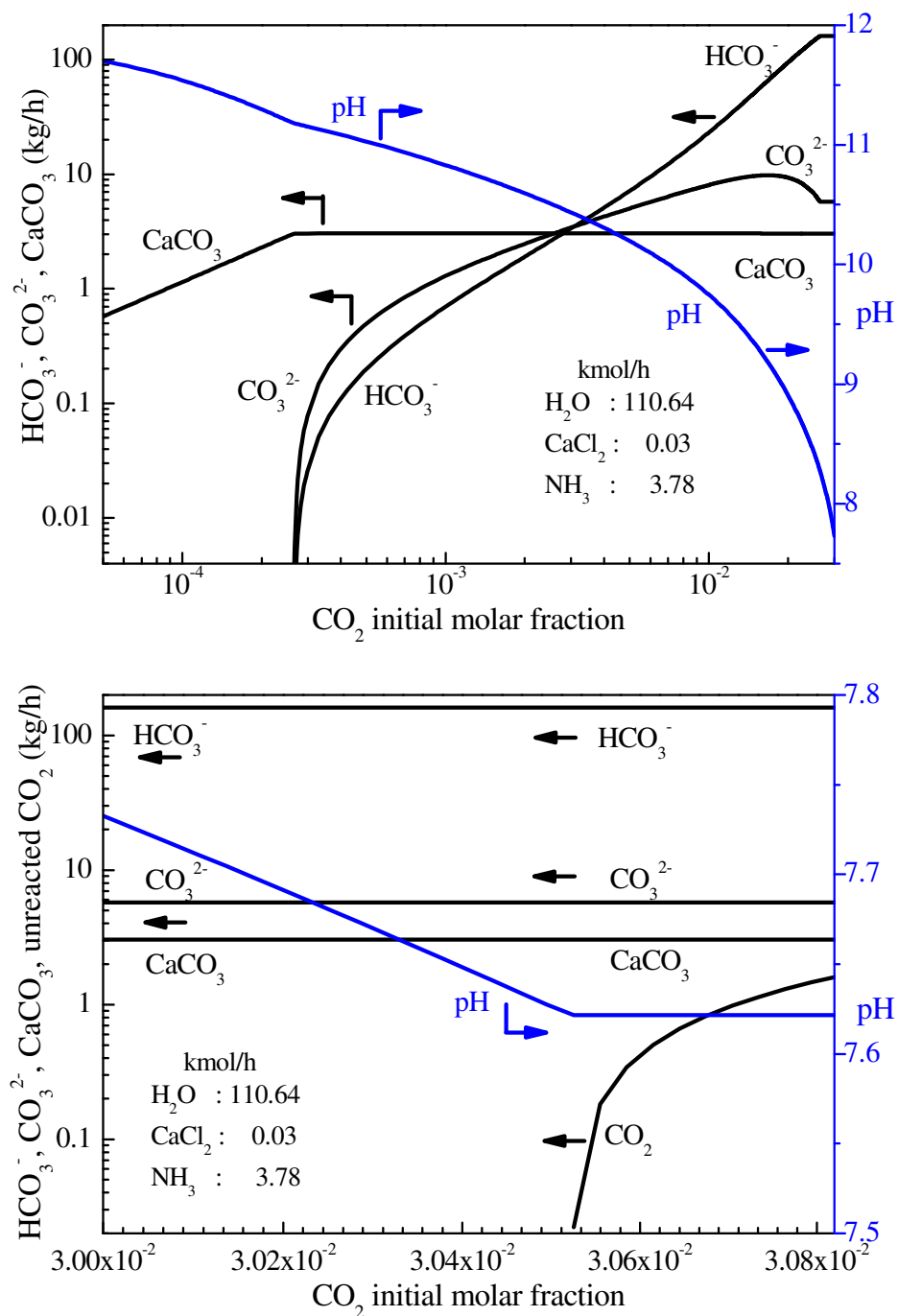



Figure 3-7. pH and production of  $\text{CaCO}_3$  and  $\text{CO}_2$ -related ion species ( $\text{HCO}_3^-$ ,  $\text{CO}_3^{2-}$ ) as well as any unreacted  $\text{CO}_2$  when increasing initial  $\text{CO}_2$  composition.



	Title <b>Report on the individual units models</b>	Deliverable number <b>D6.3</b>
		Version <b>3.1</b>

Measurement of system's pH is an indicator of the degree of  $\text{CaCO}_3$  production and the physical absorption of  $\text{CO}_2$  through its dissociation into (bi)carbonate ion species: the dissociation of an acid gas, such as  $\text{CO}_2$ , results to a decrease of system's pH. First of all, the pH measurement may indicate the global maximum of  $\text{CaCO}_3$ , which occurs at  $\text{pH}=10.85$ . pH keeps decreasing down to 7.62 (and becomes steady afterwards) when  $\text{CO}_2$  does not further react. The above analysis hints both computational optimization procedure and experimental indicators by correlating the pH with  $\text{CaCO}_3$  production and keeping track of the pH measurements during experiments, respectively.

	Title Report on the individual units models	Deliverable number <b>D6.3</b>
		Version <b>3.1</b>

## Appendix B - Additional equations for the membrane-based crystallization and method of solution

The inclusion of a varying parameter in the equations requires an extra equation; as Qin & Cabral noted this can be resolved by including a macroscopic mass balance in the shell side for the two different operating modes [28]:

$$Q_l (C_{s,z} - C_s^*) = Q_g (C_0 - C_{mc}(z)) \quad \text{Co-current mode} \quad (10)$$

$$Q_l (C_s^* - C_{s,z}) = Q_g (C_0 - C_{mc}(z)) \quad \text{Counter-current mode} \quad (11)$$

where  $Q_g$ ,  $Q_l$  are the flowrates of the gas (lumen side) and the liquid (shell side), respectively,  $C_z$  is the lumen mixed-cup concentration, and  $C_s^*$  the shell-side concentration at the module end where the lumen fluid enters regardless of the mode of operation [28].

It must be noted that along with assumptions (a)-(g), apart from gas-liquid membrane systems the aforementioned set of equations can be directly applied to various membrane systems, such as supported liquid membranes, membrane-based extraction, permabsorption, pervaporation, perstraction, etc [28].

Following Cooney et al. [29] and Qin & Cabral [28] the dimensionless variables

$$r^* = r/R_f, C^* = (C - mC_s^*) / (C_0 - mC_s^*), z^* = zD / (4uR_f^2) = 1/N_{Gz}, Sh_W = 2K_{ext}R_f/D \quad (12)$$

are introduced, so that the preceding system of partial differential equations is rendered dimensionless:

$$(1 - r^{*2}) \cdot \frac{\partial C^*}{\partial z^*} = \frac{2}{r^*} \cdot \frac{\partial C^*}{\partial r^*} + 2 \cdot \frac{\partial^2 C^*}{\partial r^{*2}} \quad (13)$$

$$C^*(0, r^*) = 1 \quad (14)$$

$$\frac{\partial C^*}{\partial r^*} \Big|_{z^*=0} = 0 \quad (15)$$

$$\frac{\partial C^*}{\partial r^*} \Big|_{z^*=1} = -\frac{Sh_W}{2} \cdot [C^*(z^*, 1) + m^*(C_{mc}^* - 1)] \quad (16)$$


where  $m^*$  is the adjusted equilibrium coefficient defined as [28]:

$$m^* = mQ_g/Q_l \text{ (co-current)} \mid m^* = -mQ_g/Q_l \text{ (counter-current)} \quad (17)$$

$C_{mc}^*$  is the dimensionless lumen mixed-cup concentration depending only on  $z^*$  and defined as:

$$C_{mc}^*(z^*) = \frac{C_{mc}(z) - mC_s^*}{C_0 - mC_s^*} = 4 \int_0^1 (1 - r^{*2}) r^* C^*(z^*, r^*) dr^* \quad (18)$$

The removal efficiency of the absorption process is given by the difference of the gas flowrates [17]:

	Title <b>Report on the individual units models</b>	Deliverable number <b>D6.3</b>
		Version <b>3.1</b>

$$\text{CO}_2 \text{ Removal} = \frac{Q_{g,in} - Q_{g,out}}{Q_{g,in}} \quad (19)$$


The system of Equations (13)-(18) comprise a PDEs set with integro-differential BC at the fiber wall, which cannot be accurately solved by difference methods, especially when accounting for the non-linear expressions of the logarithmic averaged Sherwood numbers [10, 17]. In this study, discretisation in both  $z^*$ ,  $r^*$  directions is applied, which leads to a system of algebraic equations. gPROMS ModelBuilder 5.1.1 process modelling environment was chosen for automatic discretisation and simulation of the PDE system.

Although not necessary for the same experimental set, when solving for different operating conditions (adjusting to an already solved set) the model is initialised by solving a simpler model, e.g. the linear case ( $m^*=0$ ), and then presetting the solution variables as an initial-guess matrix for the problem with the actual  $m^*$  value for fast (and successful) convergence. For the simulation the orthogonal collocation on finite elements method is chosen using 64 collocation points in each ( $r^*$ ,  $z^*$ ) domain.

In order to calculate the combined shell and membrane coefficient,  $K_{ext}$ , and enhancement factor,  $E$ , experimental data are used. Since there are two unknown parameters the problem can be set and solved as an iterative procedure. Introducing the *Obj.func* expressed as:


$$Obj.func = \left( 1 - \frac{y_{out,exp}}{y_{out,sim}} \right)^2 \quad (20)$$

the problem is rendered an optimization procedure with respect to Eq. (20) which has to be minimized by finding a suitable (optimal) set of  $K_{ext}$  and  $E$ .


	Title <b>Report on the individual units models</b>	Deliverable number <b>D6.3</b>
		Version <b>3.1</b>

## Nomenclature

$C$	concentration of the diffusing component ( $\text{mol}/\text{cm}^3$ )
$C^*$	dimensionless concentration of the diffusing component
$C_0$	lumen initial concentration of the diffusing component ( $\text{mol}/\text{cm}^3$ )
$C_{s,z}$	shell bulk concentration of the diffusing component ( $\text{mol}/\text{cm}^3$ )
$C_{mc}^*$	dimensionless mixed-cup concentration of the diffusing component
$D$	diffusion coefficient of the diffusing component ( $\text{cm}^2/\text{s}$ )
$E$	enhancement factor
$H_{\text{CO}_2}$	Henry's constant for $\text{CO}_2$ in water ( $\text{mol}/\text{atm}/\text{cm}^3$ )
$K_{\text{ext}}$	combined (shell and membrane) mass transfer coefficient ( $\text{cm}/\text{s}$ )
$M$	equilibrium coefficient including reaction
$m^*$	adjusted equilibrium coefficient
$N_{\text{Gz}}$	Graetz number, reciprocal of $z^*$
$Q_g$	total gas mixture volumetric flow rate through the lumen side ( $\text{cm}^3/\text{s}$ )
$Q_l$	total liquid volumetric flow rate through the shell side ( $\text{cm}^3/\text{s}$ )
$R$	gas constant ( $82.057 \text{ atm}\cdot\text{cm}^3/\text{mol}/\text{K}$ )
$R_f$	fiber radius ( $\text{cm}$ )
$R_m$	total mass transfer resistance in the membrane including wetting ( $\text{s}/\text{cm}$ )
$R_s$	mass transfer resistance in the shell side ( $\text{s}/\text{cm}$ )
$r$	radial distance ( $\text{cm}$ )
$r^*$	dimensionless radial distance


	Title Report on the individual units models	Deliverable number <b>D6.3</b>
		Version <b>3.1</b>

$Sh_w$	Sherwood number at the fiber wall
$T$	temperature (K)
$u$	lumen average velocity (cm/s)
$y_{CO_2,in}$	feed molar fraction of $CO_2$ in the lumen side
$y_{CO_2,out}$	outlet molar fraction of $CO_2$ in the lumen side
$z$	axial distance (cm)
$z^*$	dimensionless axial distance


	Title Report on the individual units models	Deliverable number <b>D6.3</b>
		Version <b>3.1</b>

## References

1. Chhim, N., Kharbach, C., Neveux, T., Bouteleux, C., Teychené, S., Biscans, B., Inhibition of calcium carbonate crystal growth by organic additives using the constant composition method in conditions of recirculating cooling circuits, *J. Cryst. Growth* 472 (2017) 35-45.
2. Myerson, A.S., *Handbook of Industrial Crystallization*, 2002, 2<sup>nd</sup> Ed., Butterworth-Heinemann.
3. Al-Malah, K.I.M., *ASPEN PLUS® Chemical engineering applications*, John Wiley & Sons, 2017.
4. *Aspen Plus User Guide*, AspenTech.
5. Chen, C.-C., Britt, H.I., Boston, J.F., Evans, L.B., Local compositions model for excess Gibbs energy of electrolyte systems. Part I: Single solvent, single completely dissociated electrolyte systems, *A.I.Ch.E. J.* 28 (1982) 588–596.
6. Chen, C.-C., Evans, L.B., A local compositions model for excess Gibbs energy of aqueous electrolyte systems, *A.I.Ch.E. J.* 32 (1986) 444-454.
7. Mock, B., Evans, L.B., Chen, C.-C., Thermodynamic representation of phase equilibria of mixed-solvent electrolyte systems, *A.I.Ch.E. J.* 32 (1986) 1655-1664.
8. Gabelman, A., Hwang, S.-T., A theoretical study of dense gas extraction using a hollow fiber membrane contactor, *J. Supercrit. Fluid.* 37 (2006) 157-172.
9. Pantoleontos, G., Kaldis, S.P., Koutsonikolas, D., Grammelis, P., Sakellariopoulos, G.P., CO<sub>2</sub> absorption in a mini-module membrane contactor included in Dincer, I., Hepbasli, A., Midilli, A., Karakoc, T.H. (Eds.), *Global Warming*. Springer Science+Business Media, LLC, 2010, pp. 307–313.
10. Pantoleontos, G., Kaldis, S.P., Koutsonikolas, D., Skodras, G., Sakellariopoulos, G.P., Analytical and numerical solutions of the mass continuity equation in the lumen side of a hollow-fiber membrane contactor with linear or nonlinear boundary conditions, *Chem. Eng. Commun.* 197 (2010) 709-732.
11. Di Profio, G., Salehi, S.M., Curcio, E., Drioli, E., 3.11. Membrane crystallization technology included in Drioli, E., Giorno, L., Fontananova, E. (Eds.), *Comprehensive membrane science and engineering*, Vol. 3, *Membranes in chemical/energy conversion and membrane contactors*, 2017, pp. 297-317.
12. Rongwong, W., Boributh, S., Assabumrungrat, S., Laosiripojana, N., Jiraratananon, R., Simultaneous absorption of CO<sub>2</sub> and H<sub>2</sub>S from biogas by capillary membrane contactor, *J. Membrane Sci.* 392-393 (2012) 38-47.
13. Kooijman, J.M., Laminar heat or mass transfer in rectangular channels and in cylindrical tubes for fully developed flow: comparison of solutions obtained for various boundary conditions, *Chem. Eng. Sci.* 28 (1973) 1149-1160..


	Title Report on the individual units models	Deliverable number <b>D6.3</b>
		Version <b>3.1</b>

14. Huang, C.-R., Matlosz, M., Pan, W.-D., Snyder Jr, W., Heat transfer to a laminar flow fluid in a circular tube, A.I.Ch.E. J. 30 (1984) 833-835.
15. Yao, K., Qin, Y., Yuan, Y., Liu, L., He, F., Wu, Y., A continuous-effect membrane distillation process based on hollow fiber AGMD module with internal latent-heat recovery, A.I.Ch.E. J. 59 (2013) 1278-1297.
16. Knudsen, J.G., Katz, D.L., Fluid Dynamics and Heat Transfer, McGraw-Hill, New York, 1958.
17. Pantoleontos, G., Theodoridis, T., Mavroudi, M., Kikkinides, E.S., Koutsonikolas, D., Kaldis, S.P., Pagana, A.E., Modelling, simulation, and membrane wetting estimation in gas-liquid contacting processes. Can. J. Chem. Eng. 95 (2017) 1352-1363.
18. Mavroudi, M., Kaldis, S.P., Sakellaropoulos, G.P., Reduction of CO<sub>2</sub> emissions by a membrane contacting process, Fuel 82 (2003) 2153-2159.
19. Asimakopoulou, A.G., Karabelas, A.J., Mass transfer in liquid-liquid membrane-based extraction at small fiber packing fractions, J. Membrane Sci. 271 (2006) 151-162.
20. Versteeg, G.F., van Swaaij, W.P.M., Solubility and diffusivity of acid gases (CO<sub>2</sub>, N<sub>2</sub>O) in aqueous alkanolamine solutions, J. Chem. Eng. Data 33 (1988) 29-34.
21. Shah, R.K., London, A.L., Laminar Flow Forced Convection in Ducts, Academic Press, 1978.
22. Domingues, L., Pinheiro, C.I.C., Oliveira, N.M.C., Optimal design of reactive distillation systems: Application to the production of ethyl *tert*-butyl ether (ETBE), Comput. Chem. Eng. 64 (2014) 81-94.
23. Kang, J.-L., Wong, D.S.-H., Jang, S.-S., Tan, C.-S., A comparison between packed beds and rotating packed beds for CO<sub>2</sub> capture using monoethanolamine and dilute aqueous ammonia solutions, Int. J. Greenh. Gas Con. 46 (2016) 228-239.
24. Dutta, R., Nord, L.O., Bolland, O., Prospects of using equilibrium-based column models in dynamic process simulation of post-combustion CO<sub>2</sub> capture for coal-fired power plant, Fuel 202 (2017) 85-97.
25. Hu, X., Cheng, H., Kang, X., Chen, L., Yuan, X., Qi, Z., Analysis of direct synthesis of dimethyl carbonate from methanol and CO<sub>2</sub> intensified by in-situ hydration-assisted reactive distillation with side reactor, Chem. Eng. Process. 129 (2018) 109-117.
26. Oko, E., Ramshaw, C., Wang, M., Study of intercooling for rotating packed bed absorbers in intensified solvent-based CO<sub>2</sub> capture process, Appl. Energ. 223 (2018) 302-316.
27. Braz, C.G., Mendes, A., Rocha, J., Alvim, R., Matos, H.A., Model of an industrial multitubular reactor for methanol to formaldehyde oxidation in the presence of catalyst deactivation, Chem. Eng. Sci. 195 (2019) 347-355.
28. Qin, Y., Cabral, J.M.S., Lumen mass transfer in hollow-fiber membrane processes with constant external resistances, A.I.Ch.E. J. 43 (1997) 1975-1988.

	Title Report on the individual units models	Deliverable number <b>D6.3</b>
		Version <b>3.1</b>

29. Cooney, D.O., Kim, S-S., Davis, E.J., Analyses of mass transfer in hemodialyzers for laminar blood flow and homogeneous dialysate, Chem. Eng. Sci. 29 (1974) 1731-1738.



	Title Report on the individual units models	Deliverable number <b>D6.3</b>
		Version <b>3.1</b>

## 4 Electrochemical cell model

In this section a working model for the simulation of the electrochemical conversion of carbon dioxide to formate/formic acid is presented in detail. The model consists of a combination of sub-models for the electrolyte and membrane molar transportation, the bulk reactions, the electrochemical reactions and the electric current conduction. The second part of this section reports progress related to the experimental and numerical characterization of porous electrocatalysts.

The electrochemical cell model is developed by combining individual mathematical sub-models of interacting physical and electrochemical mechanisms. The modelling approach is largely based on the work of Morrison et al. [1] and it takes into account

- (a) the bulk equilibrium reactions involving CO<sub>2</sub>, water, and the corresponding ionic species
- (b) the diffusion of species (CO<sub>2</sub>, ions) from the bulk electrolyte to the cathode surface
- (c) the electrochemical reaction kinetics of CO<sub>2</sub> to formate (and side-products) on the cathode surface

An outline of the modelling approach is depicted in Figure 4.1, where the physico-electro-chemical problem is described within the catholyte tank of an electrochemical cell for the particular case of formate production. In the right hand side, the Bulk Electrolyte represents the amount of the electrolyte, at a sufficiently large distance away from the electrode so that it can be considered unaffected by the reactions occurring on the electrode. As the distance decreases the species concentrations start to deviate from their equilibrium values. This zone is considered as the Diffusion Layer. The Electrode represents the electrochemical conversion of the species taking place on the electrode surface of the cell.

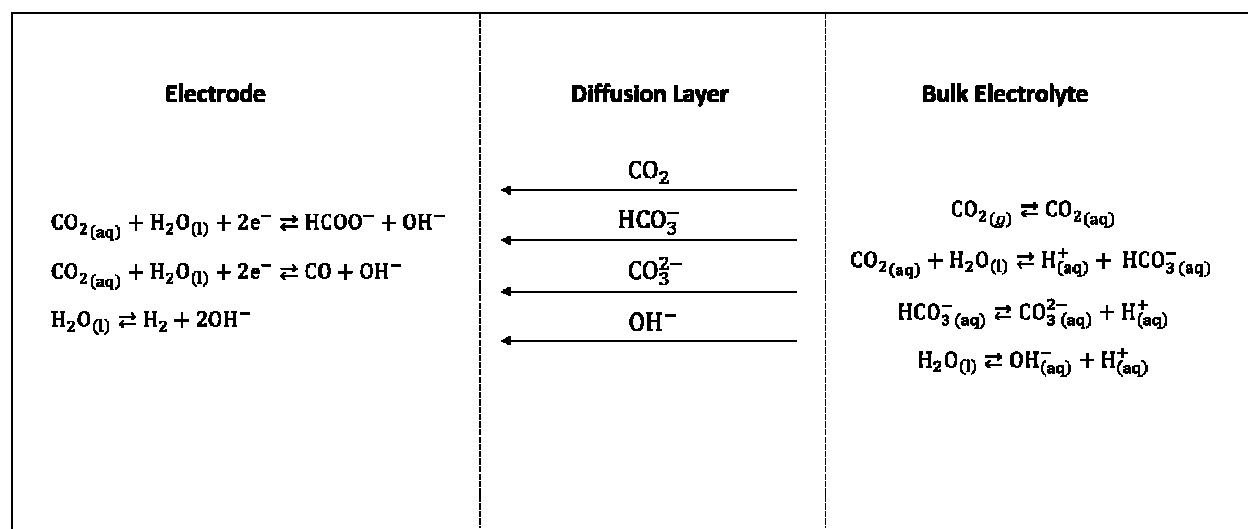



Figure 4.1 Schematic description of the electrochemistry model

	Title <b>Report on the individual units models</b>	Deliverable number <b>D6.3</b>
		Version <b>3.1</b>

### Bulk Electrolyte

In the catholyte tank, CO<sub>2</sub> gas mixes with a 0.5M KHCO<sub>3</sub> aqueous solution. The equilibrium chemistry in the Bulk Electrolyte has been simulated using the commercial ASPEN software and its thermochemistry. The reactions considered for the equilibrium calculation of the CO<sub>2</sub>-water-KHCO<sub>3</sub> system are presented in Table 4-1. The equilibrium constants ( $K_{eq}$ ) for each reaction are calculated with the following correlation.

$$\ln(K_{eq}) = A + \frac{B}{T/K} + C \ln(T) \quad (4.1)$$

with temperature T in Kelvin.

Table 4-1: Equilibrium reactions considered and coefficients used for the equilibrium constant calculation

Reaction	A	B	C
$\text{CO}_{2(g)} \rightleftharpoons \text{CO}_{2(aq)}$	Henry's Law is applied		
$\text{CO}_{2(aq)} + \text{H}_2\text{O}_{(l)} \rightleftharpoons \text{H}^+_{(aq)} + \text{HCO}_3^-_{(aq)}$	231.46	-12092.10	-36.78
$\text{HCO}_3^-_{(aq)} \rightleftharpoons \text{CO}_3^{2-}_{(aq)} + \text{H}^+_{(aq)}$	216.05	-12431.70	-35.482
$\text{H}_2\text{O}_{(l)} \rightleftharpoons \text{OH}^-_{(aq)} + \text{H}^+_{(aq)}$	132.90	-13445.90	-22.477

### Diffusion Layer

The species assumed to diffuse through the diffusion layer are CO<sub>2</sub>, HCO<sub>3</sub><sup>-</sup>, CO<sub>3</sub><sup>2-</sup>, and OH<sup>-</sup>. The diffusion of these species is governed by the Nernst-Planck equation, which describes the mass transfer to an electrode. For one-dimensional mass transfer along the x-axis, the flux  $J_i \left( \frac{\text{mol}}{\text{s m}^2} \right)$  of the species  $i$  at distance  $x$  from the electrode surface is given by the equation


$$J_i(x) = -D_i \frac{\partial C_i(x)}{\partial x} - \frac{z_i F}{RT} D_i C_i \frac{\partial \phi(x)}{\partial x} + C_i v(x) \quad (4.2)$$

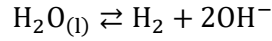
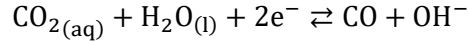
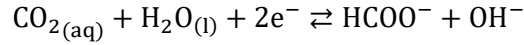
where  $D_i$  is the Fick's diffusion coefficient (m<sup>2</sup>/s) of the  $i$ -th species,  $C_i$  is the molar concentration (M),  $\phi$  is the electric potential (J),  $F$  is the Faraday constant,  $u$  is the mobility of the ionic species (m/s) and  $z_i$  is the electric charge of the ionic species.

In the Nernst-Planck equation, the first term of the right hand side represents diffusion, the second term migration while the third one represents convection. It is assumed that stirring and vibrations are avoided in the electrochemical cell, making the convection term contribution negligible. Further, migration is minor because CO<sub>2</sub>, which is the most important species for this problem, is uncharged. As a result, the diffusion term dominates the Nernst-Planck equation.

### Electrode

Carbon dioxide reduction to formate takes place on the electrode surface. However, other species are also reduced on the electrode surface competing with formate formation, which is the desired reaction. The reduction reactions considered here are described below

	Title <b>Report on the individual units models</b>	Deliverable number <b>D6.3</b>
		Version <b>3.1</b>



The partial current associated with each redox reaction under a set of conditions is indicative of the magnitude of the reaction, which determines the efficiency of the electrochemical cell. Various parameters affect the partial current, among which are the potential applied, temperature, species concentration and the number of electrons required by the reactions.

It is more convenient to work with partial current density  $j_i$  ( $\text{A}/\text{m}^2$ ) which is the partial current divided by the electrode surface area. The partial current density can be related with the species flux through the electrode surface via the equation

$$J_i(x=0) = -D_i \frac{\partial C_i(x=0)}{\partial x} = \pm \frac{\nu_m j_i}{Fn_i} \quad (4.3)$$

where  $\nu_m$  is the stoichiometric coefficient of the species, + if it is a reactant and – if it is product of the reaction and  $n_i$  is the number of electrons involved in the reaction.

The Butler-Volmer equation provides the current-potential characteristic of the electrochemical system for the  $i$ -reaction [2]

$$j_i = n_i F k_i \left[ c_o(0, t) \exp\left(-\frac{a_i n_i F}{RT} (E - E^0)\right) - c_r(0, t) \exp\left(\frac{(1-a_i) n_i F}{RT} (E - E^0)\right) \right] \quad (4.4)$$


which is fundamental for the description of the system. In (4.4)  $E$  is the applied potential and  $E^0$  is the equilibrium potential for a given reaction according to standard potentials at pH 7.

In order to obtain the current-potential characteristic, the charge transfer coefficient  $\alpha$  and the standard rate constant  $k_i$  have to be obtained for each reduction reaction. In order to approximate these two parameters, information by the experiments performed by Todoroki et al. [2] is used. Using the results for each reaction in the region where current increases exponentially with potential – i.e. before the electrochemical conversion becomes mass transfer limited – a matching of the  $\alpha$  and  $k_i$  was carried out so as to minimize error against the experimental data.

Once the current of each reaction is predicted, the Faradaic efficiency, which is an indicative magnitude of the selectivity of species  $i$ , can be calculated by the expression below

$$FE_i = \frac{j_i}{j_{total}}, \quad (4.5)$$

where  $j$  ( $\frac{\text{A}}{\text{m}^2}$ ) is the current density and  $j_{total}$  the sum of the current densities for all three reduction reactions.

	Title Report on the individual units models	Deliverable number <b>D6.3</b>
		Version <b>3.1</b>

## 4.1 Results and discussion

The coupled equations (4.1) – (4.4) are solved in MATLAB with the pdepe command. The model results are compared with literature data and shown in Figure 4.2 for current density variation as a function of applied voltage at 5 bar.

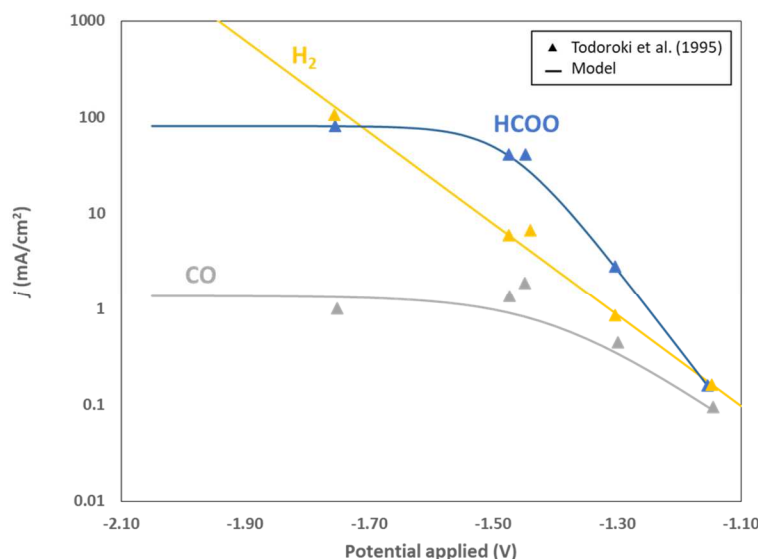



Figure 4.2 Comparison between predicted and experimentally determined [2] current density distribution among products in a CO<sub>2</sub> electrochemical cell at  $p = 5$  bar

The model is capable to simulate electrochemical conversion operating under a wide range of pressures and dominated by diffusion limited phenomena, in which cases the obtained current density varies significantly. Results indicate that in both cases the CO<sub>2</sub> electrochemical reduction is mass transfer limited under this potential range.

This working model for the electrochemical reduction of carbon dioxide can be adapted for the two electrochemical processes of the RECODE project i.e. for both formation and oxalation. A summary of the expected output of the scaled-up processes has been prepared, including information exchanged between the partners involved (AVT, CERTH, ERIC, RUG), and is presented in Table 4.2.

Regarding oxalation, in which the CO<sub>2</sub> is dissolved into the electrolyte under high pressure (10 bar), the fundamentals of the process are adequately represented by the above model, as the dissolved CO<sub>2</sub> is flowing towards the electrode. During oxalation the CO<sub>2</sub> is converted primarily to oxalate, as well as to carbon monoxide and carbonate ions. For the formate production, the physico-electro-chemical working model will be adapted to the characteristics of the process. The main difference in this case is that there is no initial compression and dissolution of the carbon dioxide into the electrolyte. Contrariwise, gas diffusion electrodes (GDE) are utilized with the intention of overcoming the mass transfer limitations arising, which may significantly decrease the efficiency of the electrochemical conversion. The model will assume that CO<sub>2</sub> is quickly dissolved in the electrolyte before the onset of the electrochemical reaction. In that sense the only difference between the two models is the specification of the CO<sub>2</sub> dissolution near the electrode surface.

	Title Report on the individual units models	Deliverable number <b>D6.3</b>
		Version <b>3.1</b>


The data in Table 4.2 will be used for the simulation of the scaled-up oxalation and formation processes, taking into account the above assumption, within the system simulation of the whole RECODE plant and will be reported in D6.4.

*Table 4.2: Information summary for the oxalation and formation scaled-up processes*

	Oxalate production	Formate production
Electrode geometrical information	0.1 m <sup>2</sup>	0.6 m <sup>2</sup>
Pressure (bar)	10	Atmospheric
Temperature (°C)	Depends on ambient conditions (20-30 °C)	Depends on ambient conditions (20-30 °C)
Inlet flow (kg/h)	1.65 kg CO <sub>2</sub> /h	2.3 kg CO <sub>2</sub> /h (directly through GDE)
Inlet composition (mol/L)	Molar composition (mol/mol): 11.6% CO <sub>2</sub> , 87% acetonitrile, 1.4% TBABF <sub>4</sub>	100 % CO <sub>2</sub> in gas
Outlet flow (kg/h)	Product is not in solution (solid product is obtained) - 0.17 kg zinc oxalate/h	0.5 kg/h formate
Outlet composition (mol/L)	Product is not in solution (solid product is obtained)	We circulate the electrolyte so the concentration will build up
Potential (V)	We will not know this until we can test the final design of the cell	We will not know this until we can test the final design of the cell
Current density (A/m <sup>2</sup> )	50 - 60mA/cm <sup>2</sup>	100-150 mA/cm <sup>2</sup>
Faradaic efficiency (%)	70-100%	70-100%
Dominant Electrochemical reactions involved	CO <sub>2</sub> ----> oxalate	CO <sub>2</sub> ----> formate
	CO <sub>2</sub> ----> CO, CO <sub>3</sub> <sup>2-</sup>	H <sup>+</sup> ----> H <sub>2</sub>

## 4.2 Membrane characterization

The present section describes the development of a porous nanostructure computational characterization tool by CERTH, e.g. [3], that can be used for membrane and electrode parameter estimation. The tool is based on the generation of 3-D digital samples of potential membrane designs based on discrete particle deposition algorithms.

	Title Report on the individual units models	Deliverable number <b>D6.3</b>
		Version <b>3.1</b>

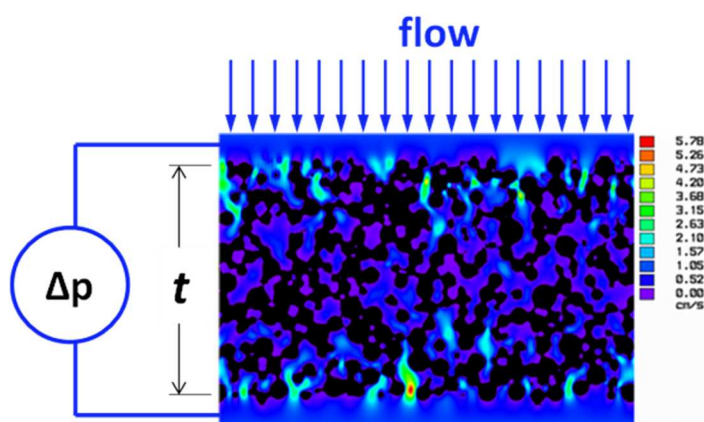


Figure 4.5. Typical velocity distribution across a membrane section

The model membrane microstructures obtained can be used for the derivation of reduced models for averaged macroscopic properties based on depth-wise functions of microstructure characteristics. The derived quantities refer either to distributions of geometric characteristics (e.g. specific surface, pore size distribution, intra-electrode pore size variation (gradient structure)) and/or to transport properties of the microporous electrode membrane (e.g. intra-electrode flow permeability).

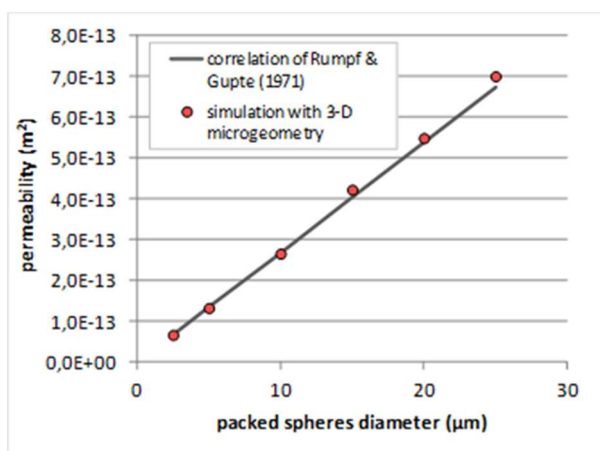



Figure 4.6. Predicted and measured permeability as a function of packed spheres diameter.

As an example consider the calculation of the Darcian permeability. This can be obtained by imposing a certain average flow velocity through a representative sample of the membrane and solving the incompressible viscous flow equations. Depthwise profile of permeability can be obtained by extracting the pressure gradient across the layer, as demonstrated in Fig. 4.5. A typical result is shown in Fig. 4.6 for the variation of permeability in a packed bed as a function of packed spheres diameter.

### 4.3 Electrocatalyst characterization

In a related work POLITO and IIT developed and characterized mesoporous nanostructured SnO<sub>2</sub> electrocatalysts that can be used for the electrochemical reduction of carbon dioxide to formic acid [4]. The highly crystalline SnO<sub>2</sub> is composed of nanoparticles with 8–20 nm in size, as shown in Fig. 4.7.

	Title Report on the individual units models	Deliverable number <b>D6.3</b>
		Version <b>3.1</b>

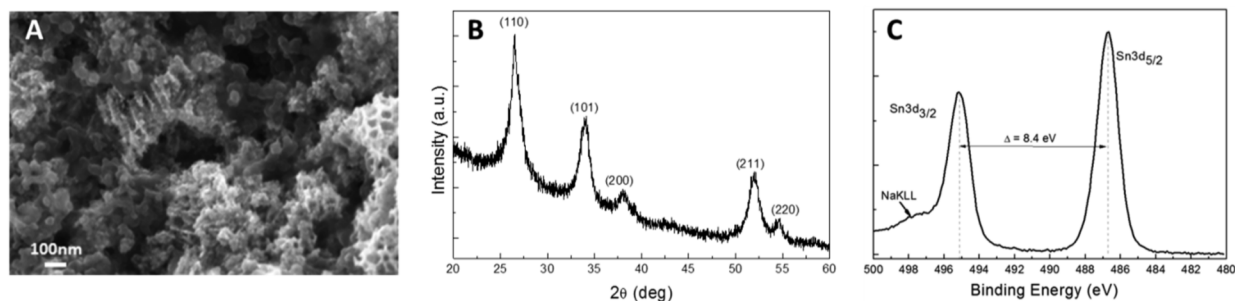


Figure 4.7.  $\text{SnO}_2$  mesoporous nanostructured electrocatalyst for  $\text{CO}_2$  electrochemical reduction.

The catalyst was shown to have superior characteristics compared to similar tin oxide commercial catalysts, as shown in Fig. 4.8, including high selectivity towards  $\text{HCOOH}$  and high stability.

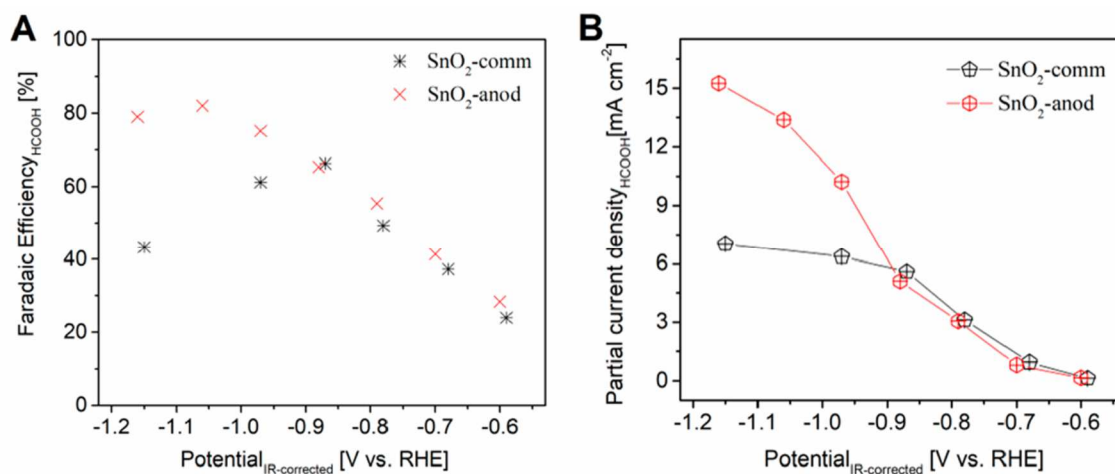



Figure 4.8. Performance of commercial and customized  $\text{SnO}_2$  electrodes.

	Title Report on the individual units models	Deliverable number <b>D6.3</b>
		Version <b>3.1</b>

## References

1. Morrison, A.R.T., van Beusekom, V., Ramdin, M., van den Broeke, L.J.P., Vlugt, T.J.H., de Jong, W. Modeling the electrochemical conversion of carbon dioxide to formic acid or formate at elevated pressures. *J. Electrochem. Soc.* 166 (2019) E77.
2. Todoroki, M., Hara, K., Kudo, A., Sakata, T. Electrochemical reduction of high pressure CO<sub>2</sub> at Pb, Hg and In electrodes in an aqueous KHCO<sub>3</sub> solution. *J. Electroanal. Chem.* 394 (1995) 199–203.
3. G. Kastrinaki, E. Daskalos, C. Pagkoura, N. D. Vlachos, G. Skevis, A.G. Konstandopoulos, M. Vardavoulas, M. Jaén, G. Saracco (2015) Synthesis and numerical simulation of nanostructured transparent conductive oxide membranes for water splitting at low-temperatures. *14th Conference of the European Ceramic Society*.
4. K. Bejtka, J. Zeng, A. Sacco, M. Castellino, S. Hernández, M. A. Farkhondehfar, U. Savino, S. Ansaloni, C. F. Pirri, A. Chiodoni, Chainlike mesoporous SnO<sub>2</sub> as a well-performing catalyst for electrochemical CO<sub>2</sub> reduction, *ACS Appl. Energy Mater.* 2 (2019) 3081-3091.